

1 **Mitochondrial fission factor (MFF) is a critical regulator of**  
2 **peroxisome maturation**

3 **Josiah B. Passmore<sup>a, 1</sup>, Ruth E. Carmichael<sup>a</sup>, Tina A. Schrader<sup>a</sup>, Luis F.**  
4 **Godinho<sup>a</sup>, Sacha Ferdinandusse<sup>b</sup>, Celien Lismont<sup>c</sup>, Yunhong Wang<sup>d</sup>,**  
5 **Christian Hacker<sup>a</sup>, Markus Islinger<sup>d</sup>, Marc Franssen<sup>c</sup>, David M. Richards<sup>e</sup>,**  
6 **Peter Freisinger<sup>f</sup>, Michael Schrader<sup>a,\*</sup>**

7 <sup>a</sup> Biosciences, University of Exeter, Exeter, UK

8 <sup>b</sup> Laboratory Genetic Metabolic Diseases, Amsterdam University Medical Centre,  
9 University of Amsterdam, The Netherlands

10 <sup>c</sup> Department of Cellular and Molecular Medicine, KU Leuven, Leuven, Belgium

11 <sup>d</sup> Institute of Neuroanatomy, Medical Faculty Mannheim, University of Heidelberg,  
12 Mannheim, Germany

13 <sup>e</sup> LSI, University of Exeter, Exeter, UK

14 <sup>f</sup> Department of Pediatrics, Kreiskliniken Reutlingen, Reutlingen, Germany

15 <sup>1</sup> Present address: Division of Cell Biology, Neurobiology and Biophysics,  
16 Utrecht University, Utrecht, The Netherlands

17

18 \* Address all correspondence to Michael Schrader, College of Life and Environmental  
19 Sciences, Biosciences, University of Exeter, Geoffrey Pope Building, Stocker Road, Exeter  
20 EX4 4QD, UK

21 E-mail: [m.schrader@exeter.ac.uk](mailto:m.schrader@exeter.ac.uk) Telephone: +44 (0) 1392 725850

22

23 **Running title:** Peroxisome abnormalities in MFF-deficient cells

24 **Keywords:** Peroxisomes, mitochondria, organelle division, MFF, PEX14, redox homeostasis,  
25 pexophagy

26 **Abbreviations:** ACOX1, acyl-CoA oxidase 1; PBD, peroxisome biogenesis disorder; PED,  
27 single peroxisomal enzyme deficiency; DRP1, dynamin-related protein 1; ER, endoplasmic  
28 reticulum; FIS1, mitochondrial fission 1 protein; MFF, Mitochondrial fission factor; ROS,  
29 reactive oxygen species; PTS, peroxisome targeting signal; VLCFA, very-long-chain fatty acid.

## 30 **Abstract**

31 Peroxisomes are highly dynamic subcellular compartments with important functions in lipid and ROS  
32 metabolism. Impaired peroxisomal function can lead to severe metabolic disorders with developmental  
33 defects and neurological abnormalities. Recently, a new group of disorders has been identified,  
34 characterised by defects in the membrane dynamics and division of peroxisomes rather than by loss of  
35 metabolic functions. However, the contribution of impaired peroxisome plasticity to the  
36 pathophysiology of those disorders is not well understood. Mitochondrial fission factor (MFF) is a key  
37 component of both the peroxisomal and mitochondrial division machinery. Patients with MFF  
38 deficiency present with developmental and neurological abnormalities. Peroxisomes (and mitochondria)  
39 in patient fibroblasts are highly elongated as a result of impaired organelle division. The majority of  
40 studies into MFF-deficiency have focused on mitochondrial dysfunction, but the contribution of  
41 peroxisomal alterations to the pathophysiology is largely unknown. Here, we show that MFF deficiency  
42 does not cause alterations to overall peroxisomal biochemical function. However, loss of MFF results  
43 in reduced import-competency of the peroxisomal compartment and leads to the accumulation of pre-  
44 peroxisomal membrane structures. We show that peroxisomes in MFF-deficient cells display alterations  
45 in peroxisomal redox state and intra-peroxisomal pH. Removal of elongated peroxisomes through  
46 induction of autophagic processes is not impaired. A mathematical model describing key processes  
47 involved in peroxisome dynamics sheds further light into the physical processes disturbed in MFF-  
48 deficient cells. The consequences of our findings for the pathophysiology of MFF-deficiency and  
49 related disorders with impaired peroxisome plasticity are discussed.

## 50 **1. Introduction**

51 Peroxisomes are highly dynamic membrane-bound organelles with key functions in cellular lipid and  
52 ROS metabolism. Defects in peroxisome biogenesis and metabolic function can result in severe  
53 disorders with developmental defects and neurological abnormalities (Dorninger et al. 2017; Wanders  
54 2018). Peroxisome biogenesis disorders (PBDs) result from mutations in *PEX* genes, which encode  
55 proteins essential for peroxisomal membrane biogenesis and matrix protein import. PBDs, such as  
56 Zellweger Spectrum disorders, are usually characterised by a loss of functional peroxisomes. This  
57 impacts on multiple metabolic pathways (e.g., peroxisomal  $\alpha$ - and  $\beta$ -oxidation of fatty acids, and the  
58 synthesis of ether-phospholipids, which are abundantly present in myelin sheaths) and results in various  
59 patient phenotypes and symptoms (Braverman et al. 2016). Peroxisomal single enzyme deficiencies  
60 (PEDs) on the other hand are caused by mutations in genes encoding a specific peroxisomal  
61 enzyme/protein and usually affect one metabolic pathway or function. The most prominent example is  
62 X-linked adrenoleukodystrophy, which is caused by mutations in the *ABCD1* gene, encoding a  
63 peroxisomal ABC transporter required for the import of very-long-chain fatty acids (VLCFAs) into the  
64 organelle (Raymond et al. 1993). In addition to PBDs and PEDs, a third group of disorders has been  
65 identified, which is characterised by defects in the membrane dynamics and division of peroxisomes  
66 rather than by loss of metabolic functions (Waterham et al. 2007; Shamseldin et al. 2012; Ebberink et  
67 al. 2012; Koch et al. 2016).

68 Peroxisomes can form and multiply by growth and division, a defined multistep pathway involving  
69 membrane elongation of existing peroxisomes, constriction, and membrane fission (Schrader et al.  
70 2016). In mammals, this involves the coordinated interplay of key membrane-shaping and fission  
71 proteins such as PEX11 $\beta$ , FIS1, MFF, and DRP1 (encoded by the *DNML1* gene) (Schrader et al. 2016).  
72 The peroxisomal membrane protein PEX11 $\beta$  is involved in several steps of peroxisomal growth and  
73 division: membrane deformation to facilitate elongation (Delille et al. 2010; Opaliński et al. 2011),  
74 recruitment of the division factors MFF and FIS1 to constriction sites (Koch et al. 2005; Koch and  
75 Brocard 2012; Itoyama et al. 2013), and activation of the fission GTPase DRP1 (Williams et al. 2015).  
76 The tail-anchored membrane proteins MFF and FIS1 act as adaptor proteins for the recruitment of DRP1  
77 to the peroxisomal membrane and interact with PEX11 $\beta$  (Schrader et al. 2016). With the exception of  
78 PEX11 $\beta$ , all proteins involved in peroxisome growth and division identified so far are also key  
79 mitochondrial division factors. FIS1 and MFF are dually targeted to both peroxisomes and mitochondria,  
80 and also recruit DRP1 to the mitochondrial outer membrane (Koch et al. 2005; Gandre-Babbe and van  
81 der Bliek 2008; Costello et al. 2017a, 2018). Mitochondria also possess the adaptor proteins MiD49 and  
82 MiD51, which are specific to mitochondria and can recruit DRP1 independent of FIS1 and MFF (Palmer  
83 et al. 2013). GDAP1 is another tail-anchored membrane protein shared by mitochondria and  
84 peroxisomes, which influences organelle fission in an MFF- and DRP1-dependent manner in neurons  
85 (Huber et al. 2013). Recently, also MIRO1, a tail-anchored membrane adaptor for the microtubule-  
86 dependent motor protein kinesin, has been shown to localise to mitochondria and peroxisomes and to  
87 contribute to peroxisomal motility and membrane dynamics (Castro et al. 2018; Okumoto et al. 2018;  
88 Covill-Cooke et al. 2020).

89 Patients with mutations in DRP1/DNML1, PEX11 $\beta$ , or MFF have been identified and often present  
90 with neurological abnormalities (Waterham et al. 2007; Shamseldin et al. 2012; Ebberink et al. 2012;  
91 Costello et al. 2018). Loss of DRP1 or MFF function leads to a block in mitochondrial and peroxisomal  
92 fission resulting in highly elongated organelles with impaired dynamics. However, the metabolic  
93 functions of both peroxisomes and mitochondria are typically not or only slightly altered, indicating  
94 that changes in organelle dynamics and plasticity are the main contributors to the pathophysiology of

95 the disease (Waterham et al. 2007; Shamseldin et al. 2012; Koch et al. 2016; Yoon et al. 2016; Vanstone  
96 et al. 2016; Nasca et al. 2016; Gerber et al. 2017; Nasca et al. 2018; Ladds et al. 2018).

97 MFF deficiency displays with developmental delay, peripheral neuropathy, optic atrophy, and Leigh-  
98 like encephalopathy (Shamseldin et al. 2012; Koch et al. 2016; Nasca et al. 2018). The mitochondria in  
99 MFF-deficient patient fibroblasts show no significant alteration in oxidative phosphorylation or mtDNA  
100 (Koch et al. 2016; Nasca et al. 2018). Likewise, loss of MFF did not significantly alter the mitochondrial  
101 membrane potential, ATP levels or the redox potential of the mitochondrial matrix in neuronal cells  
102 (Lewis et al. 2018). While the majority of studies into MFF-deficiency have focused on mitochondrial  
103 dysfunction, the contribution of peroxisomal alterations to the pathophysiology is largely unknown.  
104 Similarly to DRP1 and PEX11 $\beta$  patients, it appears that peroxisomal metabolic function is unaltered  
105 (Koch et al. 2016; Nasca et al. 2018), with the only known peroxisome dysfunction being hyper-  
106 elongation. In this study, we assess the extent to which peroxisomal functions and properties are altered  
107 in MFF-deficient cells, giving further insight into the pathophysiological consequences of loss-of-  
108 function of MFF. We show that loss of MFF impacts on the distribution of peroxisomal marker proteins  
109 and causes the accumulation of pre-peroxisomal membrane structures. Furthermore, peroxisomes in  
110 MFF-deficient cells display alterations in peroxisomal redox state and intra-peroxisomal pH.  
111 Interestingly, elongated peroxisomes in MFF-deficient cells are not fully static, and their dynamics can  
112 be modulated, e.g. through the induction of autophagic processes. The consequences of our findings for  
113 the understanding of the pathophysiology of MFF-deficiency and related disorders with impaired  
114 peroxisome plasticity are discussed.

## 115 2. Materials and Methods

### 116 2.1. Plasmids, Antibodies and siRNAs

117 The plasmids and antibodies used in this study are detailed in Tables S1 and S2, respectively. PEX14  
118 siRNA (GAACUCAAGUCCGAAAUUA) (Lee et al. 2017) and MFF siRNA  
119 (GACCAGCAGAUCUUGACCU) (Long et al. 2013) were generated by Eurofins as 21-mer siRNAs  
120 with 3' dTdT overhangs. PEX5 siRNA (TriFECTa kit) was obtained from Integrated DNA  
121 Technologies. siGENOME Non-Targeting siRNA Control Pool (Dharmacon) and siMAX Non Specific  
122 siRNA Control 47% GC (AGGUAGUGUAAUCGCCUUG-TT, Eurofins) were used as controls.

### 123 2.2. Fibroblast Cell Culture and Transfection

124 For routine culture and morphological experiments, MFF-deficient patient skin fibroblasts and controls  
125 (Shamseldin et al. 2012; Koch et al. 2016) were cultured in Dulbecco's Modified Eagle Medium  
126 (DMEM), high glucose (4.5 g/L) supplemented with 10% FBS, 100 U/mL penicillin and 100 µg/mL  
127 streptomycin at 37°C (5% CO<sub>2</sub> and 95% humidity). The patient cells used have previously been shown  
128 to carry the following mutations in the MFF gene: c.C190T:p.Q64\* (Shamseldin et al. 2012);  
129 c.184dup:p.L62Pfs\*13 combined with c.C892T:p.R298\* (Koch et al. 2016; patient 1);  
130 c.453\_454del:p.E153Afs\*5 (Koch et al. 2016; patient 2). For FRAP experiments, cells transfected with  
131 EGFP-SKL were grown on 3.5-cm glass bottom dishes (Cellview; Greiner BioOne, Germany). For  
132 assessing peroxisome degradation during starvation, cells were cultured in Hanks' Balanced Salt  
133 Solution (HBSS) for the time indicated, and recovered in full DMEM. For assessing peroxisome  
134 alterations with microtubule depolymerisation, cells were treated with 10 µM Nocodazole (or 0.07%  
135 DMSO as a control), for four hours prior to fixation. MFF-deficient (MFF<sup>Q64\*</sup>) and control human  
136 fibroblasts were immortalised by introduction of the SV40 large T antigen. Immortalised fibroblasts  
137 (HUFs-T) were cultured in  $\alpha$ -modified Eagle's medium (MEM $\alpha$ ) supplemented with 10% FBS, 2 mM  
138 Ultraglutamine 1 (Lonza) and 1 $\times$  MycoZap antibiotics (Lonza) at 37°C (5% CO<sub>2</sub> and 95% humidity).  
139 Transfection of fibroblasts was performed using the Neon Transfection System (Thermo Fisher  
140 Scientific) as previously described for roGFP2 constructs (Lismont et al. 2017) and siRNA (Schrader  
141 and Schrader 2017).

### 142 2.2. Immunofluorescence and Immunoblotting

143 Unless otherwise indicated, immunofluorescence was performed 24 hours post-transfection. Cells  
144 grown on glass coverslips were fixed for 20 minutes with 4% paraformaldehyde (PFA) in PBS (pH 7.4),  
145 permeabilised with 0.2% Triton X-100 for 10 minutes and blocked with 1% BSA for 10 minutes.  
146 Blocked cells were incubated with primary and secondary antibodies sequentially in a humid chamber  
147 for 1 hour. Cells were washed 3 times with PBS between each individual step. Finally, coverslips were  
148 washed with ddH<sub>2</sub>O to remove PBS and mounted on glass slides in Mowiol 4-88-containing *n*-propyl  
149 gallate as an anti-fading (Bonekamp et al. 2013).

150 For detection of protein levels, cells were trypsinised, washed in PBS, and centrifuged at 500 $\times$ g for 3  
151 min. Cell pellets were lysed and equal amounts of protein were separated by SDS-PAGE on 12.5%  
152 polyacrylamide gels. Transfer to a nitrocellulose membrane (Amersham Bioscience, Arlington Heights,  
153 IL, USA) was performed using a semi-dry apparatus (Trans-Blot SD, Bio-rad) and analysed by  
154 immunoblotting with enhanced chemiluminescence reagents (Amersham Bioscience, Arlington  
155 Heights, IL, USA).

### 156 **2.3. Microscopy**

157 Cell imaging was performed using an Olympus IX81 microscope with an UPlanSApo 100x/1.40 Oil  
158 objective (Olympus Optical, Hamburg, Germany). Filters sets eGFP ET (470/40 Et Bandpass filter,  
159 Beamsplitter T495 LPXR and 525/50 ET Bandpass filter [Chroma Technology GmbH, Olching,  
160 Germany]), and TxRed HC (562/40 BrightLine HC Beamsplitter HC BS 593, 624/40 BrightLine HC  
161 [Semrock, Rochester, USA]) were used. Images were taken with a CoolSNAP HQ2 CCD camera.

162 Live-cell imaging of roGFP2 constructs in HUFs-T fibroblasts was performed with an Olympus IX81  
163 microscope equipped with an UPlanSApo 100x/1.40 Oil objective (Olympus Optical, Hamburg,  
164 Germany), BP390-410 and BP470-495 bandpass excitation filters, a dichromatic mirror with a cut-off  
165 at 505 nm, a BA510-550 barrier (emission) filter, and a CCD-FV2T digital black and white camera.

166 Confocal images of MFF<sup>Q64\*</sup> fibroblasts to assess peroxisomal tubule localisation with microtubules  
167 were obtained using a Zeiss LSM 880 inverted microscope, with Airyscan spatial detector array (ChA-  
168 T1 5.7, ChA-T2 6.9) for super-resolution imaging. The Alpha Plan Apochromat 100x/1.46 oil DIC M27  
169 Elyra objective was used, with lasers 561 nm (15% power) and 488 nm (3% power).

170 Confocal images of the pHRed probe in fibroblasts were obtained using a Zeiss LSM 510 META  
171 inverted microscope equipped with a Plan Apochromat 63x/1.4 NA (oil/dic) objective (Carl Zeiss),  
172 using Argon excitation 458 nm and DPSS561 excitation 561 nm, with emission collection 600–620 nm.  
173 For detection of peroxisomal pHRed (pHRed-PO) the HC PL APO CS2 63x/1.4 Oil objective was used.  
174 For live-cell imaging, cells were plated in 3.5 cm diameter glass bottom dishes (Cellview; Greiner Bio-  
175 One). MetaMorph 7 (Molecular Devices, USA) was used to adjust for contrast and brightness.

176 Photo-bleaching experiments were performed using a Visitron 2D FRAP system, consisting of a 405  
177 nm/60mW diode laser. The FRAP laser was controlled by UGA-40 controller (Rapp OptoElectronic  
178 GmbH, Hamburg, Germany) and a VisiFRAP 2D FRAP control software for Meta Series 7.5.x (Visitron  
179 System, Munich, Germany) The FRAP system was coupled into a IX81 motorized inverted microscope  
180 (Olympus, Hamburg, Germany), equipped with a PlanApo 100X/1.45 Oil objective (Olympus,  
181 Hamburg, Germany). Fluorescently-labelled proteins were visualised by using a VS-LMS4 Laser-  
182 Merge-System with solid state lasers (488 nm/75mW, Visitron System, Munich, Germany). Images  
183 were captured using a Charged-Coupled Device camera (Photometric CoolSNAP HQ2, Roper  
184 Scientific, Germany). Peroxisomes in MFF-deficient fibroblasts expressing EGFP-SKL were irradiated  
185 by using 100% output power of the 405 nm laser for 150 ms with a beam diameter of 30 pixels. This  
186 was followed by immediate observation. Further details on the methods can be found in (Schuster et al.  
187 2011a, b).

188

189 For transmission electron microscopy, fibroblast monolayers were fixed in 0.5% glutaraldehyde in 0.2  
190 M Pipes buffer, pH 7.2, for 15 min at room temperature. Cells were then scraped from the culture dish  
191 and pelleted at 17,000 g for 10 min. Following three buffer washes, the cell pellet was fragmented and  
192 postfixed for 1 h in 1% osmium tetroxide (reduced with 1.5% wt/vol potassium ferrocyanide) in 0.1 M  
193 sodium cacodylate buffer, pH 7.2. Following three 5 minute washes in distilled water, the pellet  
194 fragments were dehydrated through an ethanol gradient and embedded in Durcupan resin (Sigma-  
195 Aldrich). 70-nm ultrathin sections were collected on pioloform-coated 100-mesh copper EM grids  
196 (Agar Scientific) and contrasted with lead citrate before imaging using a JEOL JEM 1400 transmission  
197 electron microscope operated at 120 kV.

## 198 **2.4. Measurement of Peroxisomal Body Size, Tubule Size and Length, and Number**

199 The Metamorph 7 (Molecular Devices, USA) region measurements function was used for analysis of  
200 peroxisome size in MFF-deficient fibroblasts, following calibration of distances for the magnification  
201 used. For measurement of peroxisome body and tubule width, transmission EM images were used at  
202 80,000- and 100,000-fold magnification. For measurement of peroxisome length, immunofluorescence  
203 images were used at 100-fold magnification and the Metamorph 7 segmented line tool was used. For  
204 calculation of peroxisomal number in control fibroblasts, an in-house ImageJ (Schneider et al. 2012)  
205 macro was used, utilising the Analyze Particles function. For MFF-deficient patient fibroblasts,  
206 peroxisome number was counted manually.

## 207 **2.5. Marker Protein Distribution Measurements**

208 To measure the fluorescence intensity of PEX14, PMP70, catalase or EGFP-SKL over the length of a  
209 single peroxisome in fixed cells, and EGFP-SKL fluorescence following live-cell photobleaching  
210 experiments, the ImageJ (Schneider et al. 2012) Plot Profile function was used. A 2 pixel width line  
211 was drawn along the centre of the peroxisome from the body, along the tubule for a total length of 5  
212  $\mu\text{m}$ , with channels overlaid where appropriate. The fluorescence intensity for each colour channel was  
213 measured with 65 nm increments. For marker distribution measurements, data were normalised to a 0-  
214 1 scale, with 1 representing the value of the pixel with the maximum intensity of unsaturated images.  
215 For photobleaching experiments, data are presented as the mean grey value for each increment. Only  
216 peroxisomes which did not overlap with other peroxisomes were analysed.

## 217 **2.6. Metabolic and Biochemical Analyses**

218 Peroxisomal parameters were determined in cultured skin fibroblasts (Ferdinandusse et al. 2016).  
219 Concentrations of VLCFAs and C26:0 lysophosphatidylcholine (C26:0 lysoPC) were measured in  
220 cultured cells as described previously (Dacremont et al. 1995; Ferdinandusse et al. 2016). Peroxisomal  
221  $\beta$ -oxidation of the VLCFA hexacosanoic acid (C26:0) and pristanic acid were measured as described  
222 (Wanders et al. 1995). A D3-C22:0 loading test was performed by loading cells for 3 days with  
223 deuterated (D3) C22:0 followed by fatty acid analysis with tandem mass spectrometry, essentially as  
224 previously described (Kemp et al. 2004) but with D3-C22:0 instead of D3-C24:0. Peroxisomal phytanic  
225 acid  $\alpha$ -oxidation (Wanders and Van Roermund 1993) and the activity of dihydroxyacetone phosphate  
226 acyltransferase (DHAPAT), a key enzyme in peroxisomal ether phospholipid synthesis, were measured  
227 as described (Ofman and Wanders 1994). Immunoblot analysis was performed with cell homogenates,  
228 which were separated by SDS-PAGE and subsequently transferred onto a nitrocellulose membrane  
229 using semidry blotting. For visualisation, the secondary antibody IRDye 800 CW goat anti-rabbit was  
230 used with the Odyssey Infrared Imaging System (LI-COR Biosciences, Nebraska, USA).

## 231 **2.7. Measurement of Subcellular Redox Dynamics**

232 The procedures involved in the measurement of subcellular redox levels have been previously described  
233 in detail (Lismont et al. 2017). In brief, SV40 large T antigen-transformed human fibroblasts (HUFs-T)  
234 were transfected with plasmids coding for GSH/GSSG- (roGFP2) or  $\text{H}_2\text{O}_2$ -sensitive (roGFP2-ORP1)  
235 reporter proteins targeted to various subcellular compartments [cytosol (c-), mitochondria (mt-), or  
236 peroxisomes (po-)]. One day later, the cells were incubated for 30-60 minutes in phenol red-free culture  
237 medium and imaging was performed to visualize both the oxidized (excitation 400 nm, emission 515  
238 nm) and reduced (excitation 480 nm, emission 515 nm) states of roGFP2. During image acquisition,  
239 the cells were maintained in a temperature-, humidity-, and  $\text{CO}_2$ -controlled incubation chamber. For  
240 cytosolic measurements, the ROI was selected outside the nucleus. The Cell<sup>M</sup>/xcellence software

241 module (Olympus) was used to quantify the relative fluorescence intensities of roGFP2 at 400 and 480  
242 nm excitation, giving a ratiometric response.

## 243 **2.8. Measurement of Peroxisomal pH using pHRed**

244 Peroxisomal pH was measured as previously described (Godinho and Schrader 2017). Briefly, MFF-  
245 deficient and control fibroblasts were transfected with plasmids coding for a cytosolic or peroxisomal  
246 pH-sensitive red fluorescent protein (pHRed-Cyto and pHRed-PO, respectively) (Godinho and  
247 Schrader 2017). Twenty four hours after transfection, cells were imaged using excitation wavelengths  
248 of 458 and 561 nm. Prior to image acquisition, a controlled temperature chamber was set-up on the  
249 microscope stage at 37°C, as well as an objective warmer. During image acquisition, cells were kept at  
250 37°C and in a HEPES-buffered CO<sub>2</sub>-independent medium. For calibration, the cells were incubated in  
251 solutions of known pH (containing 5 μM nigericin) in a confocal stage chamber. ImageJ (Schneider et  
252 al. 2012) was used to calculate the 561/458 ratiometric response.

## 253 **2.9. Statistical Analysis**

254 Unless indicated otherwise, a two-tailed, unpaired *t*-test was used to determine statistical differences  
255 against the indicated group (\*,  $P < 0.05$ ; \*\*,  $P < 0.01$ ; \*\*\*,  $P < 0.001$ ). Boxplots are presented with the  
256 bottom and top of each box representing the 25th and 75th percentile values, respectively; the horizontal  
257 line inside each box representing the median; and the horizontal lines below and above each box  
258 denoting the range. In the roGFP (Fig. 4B) and roGFP-ORP (Fig. 4D) box plots, these lines denote the  
259 standard deviation. Bar graphs are presented as mean ± SEM. In-text data are presented as mean ± SD.  
260 Analysis was performed from at least three independent experiments.



261 **Table S1.** Plasmids used in this study

<b>Plasmid</b>	<b>Source</b>
<b>EGFP-SKL</b>	Koch et al. 2005
<b>Myc-MFF</b>	Gandre-Babbe and van der Blik 2008
<b>c-roGFP2</b>	Ivashchenko et al. 2011
<b>mt-roGFP2</b>	Ivashchenko et al. 2011
<b>po-roGFP2</b>	Ivashchenko et al. 2011
<b>c-roGFP2-ORP1</b>	Lismont et al. 2019b
<b>mt-roGFP2-ORP1</b>	Lismont et al. 2019b
<b>po-roGFP2-ORP1</b>	Lismont et al. 2019b
<b>pHRed-Cyto</b>	Godinho and Schrader 2017
<b>pHRed-PO</b>	Godinho and Schrader 2017
<b>HsPEX3(1-44)-EGFP</b>	Fransen et al. 2001

262

263 **Table S2.** Primary and secondary antibodies used in this study

<b>Antibody</b>	<b>Type</b>	<b>Dilution</b>		<b>Source</b>
		<b>IMF</b>	<b>WB</b>	
<b>ACBD5</b>	pc rb		1:1000	Proteintech (21080-1-AP)
<b>ACOX1</b>	pc rb	-	1:1000	Proteintech (10957-1-AP) or gift from T. Hashimoto, Japan
<b>ATP synthase</b>	mc ms	1:500	-	Abcam (ab14730)
<b><math>\alpha</math>-Tubulin</b>	mc ms	-	1:1000	Sigma (T9026)
<b>Catalase</b>	pc ms	1:150	-	Abcam (ab88650)
<b>Catalase</b>	mc rb	-	1:250	Abcam (ab179843)
<b>GAPDH</b>	pc rb	-	1:5000	ProSci (3783)
<b>Myc</b>	mc ms	1:200	-	Santa Cruz Biotechnology, Inc (9E10)
<b>PEX5</b>	pc rb	-	1:750	Sigma (HPA039259)
<b>PEX11<math>\beta</math></b>	mc rb		1:1000	Abcam (ab181066)
<b>PEX14</b>	pc rb	1:1400	1:4000	D. Crane, Griffith University, Brisbane, Australia
<b>PMP70</b>	pc rb	1:100	-	A. Völkl, University of Heidelberg, Heidelberg, Germany
<b>PMP70</b>	mc ms	1:500	-	Sigma (SAB4200181)

<b>Thiolase</b>	pc rb	-	1:2000	Atlas antibodies (HPA007244)
<b>Alexa Fluor 488</b>	dk anti-ms	1:500	-	ThermoFisher Scientific (A21202)
<b>Alexa Fluor 488</b>	dk anti-rb	1:500	-	ThermoFisher Scientific (A21206)
<b>Alexa Fluor 594</b>	dk anti-ms	1:500	-	ThermoFisher Scientific (A21203)
<b>Alexa Fluor 594</b>	dk anti-rb	1:500	-	ThermoFisher Scientific (A21207)
<b>HRP IgG</b>	gt anti-ms	-	1:10000	Bio-Rad (170-6516)
<b>HRP IgG</b>	gt anti-rb	-	1:10000	Bio-Rad (172-1013)
<b>IRDye 800 CW</b>	gt anti-rb	-	1:12500	Westburg

---

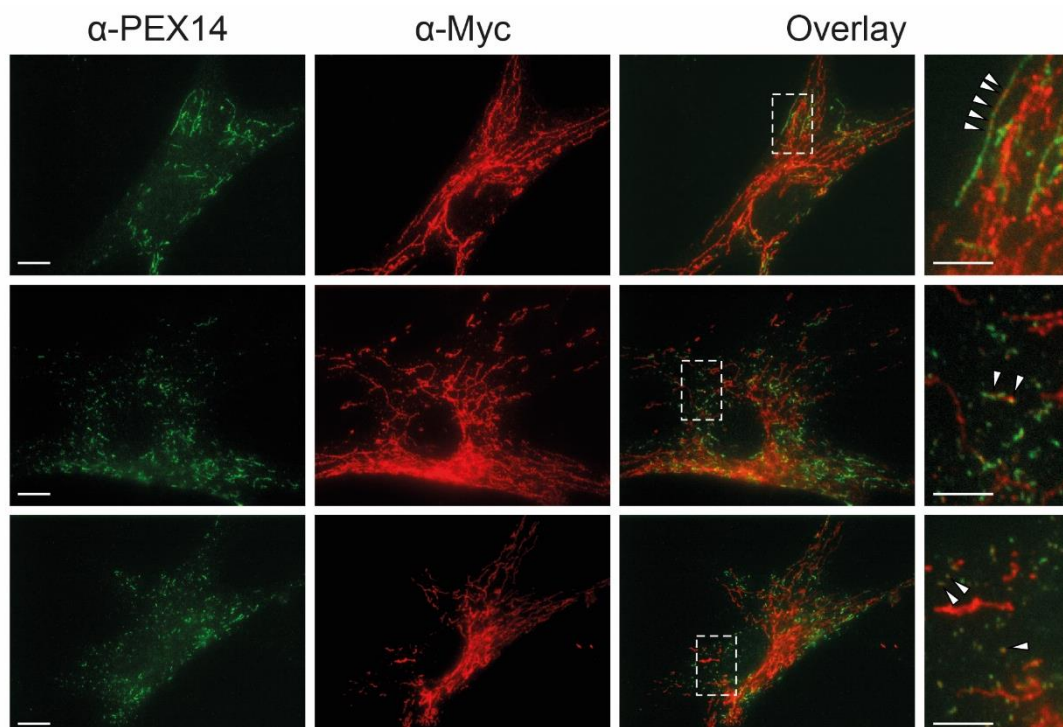
264 Abbreviations: IMF, immunofluorescence; WB, Western blot; pc, polyclonal; mc, monoclonal; ms,  
265 mouse; rb, rabbit; gt, goat; dk, donkey; HRP, horseradish peroxidase.

## 266 3. Results

### 267 3.1. Morphological characterisation of MFF-deficient peroxisomes

268 To visualize peroxisomes in different MFF-deficient patient skin fibroblasts (Shamseldin et al. 2012;  
269 Koch et al. 2016) under similar conditions, we processed the cells for immunofluorescence microscopy  
270 using an antibody against PEX14, a peroxisomal membrane protein. As previously reported, fibroblasts  
271 from all three MFF-deficient patients show highly elongated peroxisomes, whereas in controls  
272 peroxisomes showed a punctate staining pattern typical for human fibroblasts (**Fig. 1A**). Mitochondria  
273 in patient cells were also reported to be elongated (Shamseldin et al. 2012; Koch et al. 2016). In many  
274 cells peroxisomes were extremely long (> 30  $\mu\text{m}$ ); elongation was even more pronounced than in DRP1  
275 patient fibroblasts, which also display tubular peroxisomes and mitochondria (Waterham et al. 2007;  
276 Nasca et al. 2016). The elongation of peroxisomes in MFF-deficient fibroblasts has been suggested to  
277 be the result of a constant lipid flow from the ER to peroxisomes via membrane contact sites, which are  
278 mediated by peroxisomal ACBD5 and ER-resident VAPB (Costello et al. 2017b). As peroxisomes  
279 cannot divide due to the loss of functional MFF, lipid transfer from the ER results in a pronounced  
280 growth/elongation of the peroxisomal membrane. Furthermore, re-introduction of MFF has been shown  
281 to restore the normal, punctate peroxisomal phenotype in MFF-deficient fibroblasts (Costello et al.  
282 2017b). We transfected MFF-deficient fibroblasts with Myc-MFF using microporation, which allowed  
283 us to monitor peroxisome morphology at early time points (2-3 hours) after transfection and therefore  
284 capture the initial stages of MFF-mediated peroxisome division (**Suppl. Fig. S1**). Cells were processed  
285 for immunofluorescence using antibodies against the Myc-tag and PEX14. Two – three hours after  
286 transfection, MFF was observed to localise in spots on elongated peroxisomes (and elongated  
287 mitochondria) supporting a role in the assembly of the division machinery and the formation of division  
288 sites. Many MFF-expressing cells already contained short, dividing peroxisomes or fully divided,  
289 spherical peroxisomes (**Suppl. Fig. S1**).

290

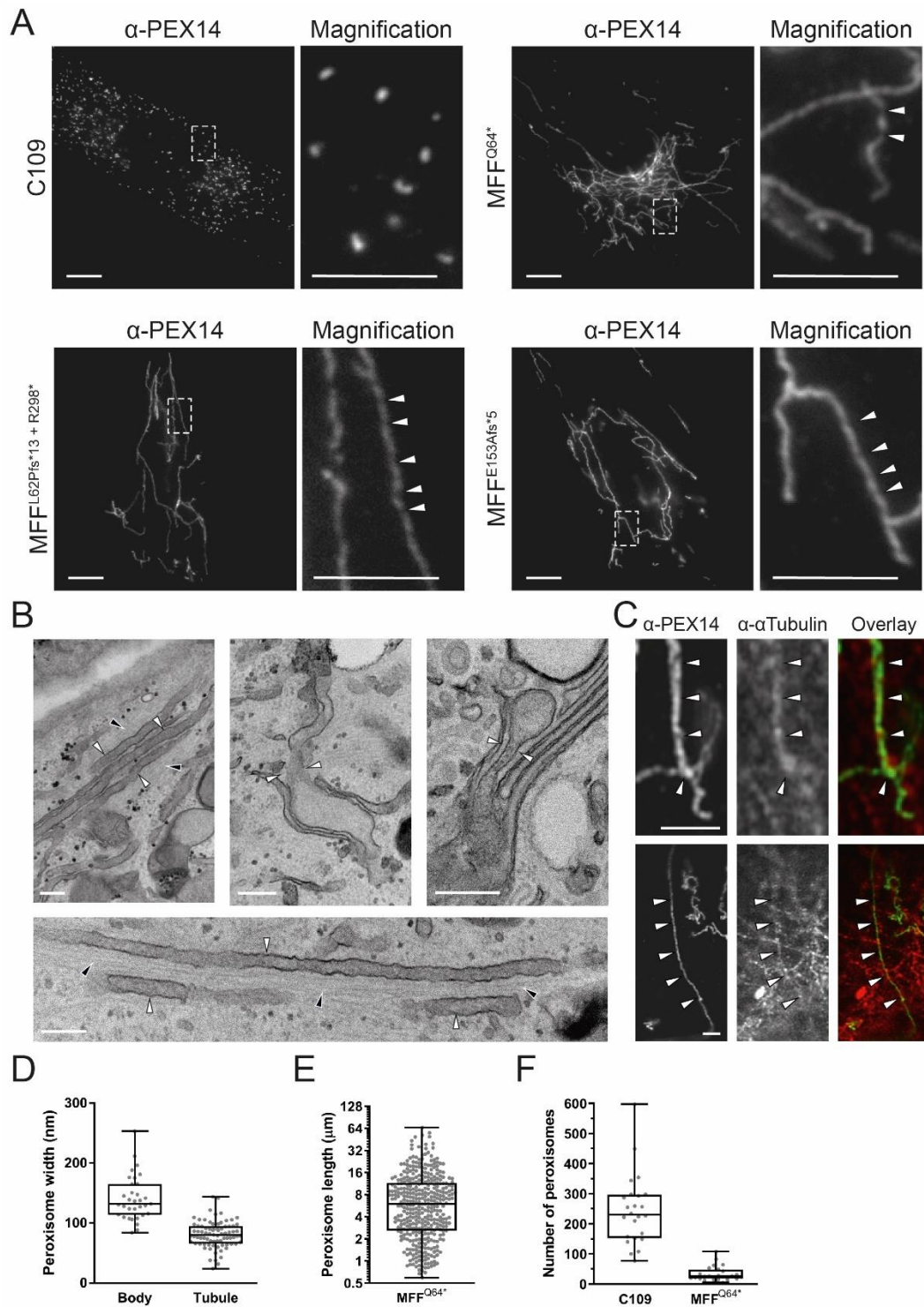


291 **Suppl. Figure S1.** Re-introduction of MFF in MFF-deficient patient fibroblasts. MFF-deficient patient  
292 fibroblasts [mutation Q64\* (Shamseldin et al. 2012)] were transfected with Myc-MFF using  
293 microporation. Cells were processed for immunofluorescence microscopy 2-3 hours after transfection  
294 using antibodies directed to the Myc-tag and PEX14, a peroxisomal membrane marker. Note the  
295 localisation of MFF in spots on elongated peroxisomes (upper panel; arrowheads), the appearance of  
296 shorter peroxisomes due to peroxisome division (middle panel), and the restoration of the normal,  
297 spherical peroxisome morphology (lower panel). Higher magnification of boxed regions is shown. Scale  
298 bars, 10  $\mu\text{m}$ ; magnification, 5  $\mu\text{m}$ .

299

300 Occasionally, peroxisomes in patient fibroblasts appeared to have a constricted, ‘beads-on-a-string’  
301 phenotype (**Fig. 1A**, Magnifications). Such a phenotype is seen with DRP1 depletion, as peroxisomal  
302 constriction can occur independently of DRP1, but fission cannot (Koch et al. 2004). How peroxisomal  
303 constriction is mediated is still unclear. A constricted, ‘beads-on-a-string’-like peroxisome morphology  
304 in MFF-deficient cells would suggest that peroxisomal constriction can also occur independently of  
305 MFF (Ribeiro et al. 2012). However, MFF is also suggested to play a role in the constriction of the  
306 peroxisomal membrane, as it localises to peroxisomal constriction sites (Itoyama et al. 2013; Soliman  
307 et al. 2018). To confirm constricted peroxisome morphology in MFF-deficient cells, we performed  
308 electron microscopy (**Fig. 1B**). In contrast to immunofluorescence, constrictions of elongated  
309 peroxisomes were not observed in ultrastructural studies (**Fig. 1B**). Interestingly, EM revealed the  
310 presence of spherical peroxisome bodies, with a single, smaller tubule protruding from the body (**Fig.**  
311 **1B**). We assume that the “constricted” appearance of peroxisomes in immunofluorescence is likely due  
312 to instability of the extremely long, delicate membrane structures during fixation with para-  
313 formaldehyde, highlighting the importance of ultrastructural studies to validate light microscopy  
314 observations. Ultrastructural studies (**Fig. 1B**) and immunofluorescence microscopy (**Fig. 1C**) show  
315 that the peroxisomal membrane tubules are frequently aligned along microtubules, which may  
316 contribute to tubule stability and maintenance.

317 Measurement of peroxisomes in EM micrographs revealed that peroxisome bodies are significantly  
318 larger than peroxisomal tubules (mean width, body:  $141 \pm 37$  nm, tubule:  $81 \pm 22$  nm) (**Fig. 1D**). The  
319 measured body width is consistent with that of spherical peroxisomes in human fibroblasts from healthy  
320 individuals typically being reported to be between 50-200 nm in width (Arias et al. 1985; Galiani et al.  
321 2016). Peroxisome length was also quantified based on immunofluorescence data, with a wide range of  
322 lengths being present, from smaller, rod shaped peroxisomes ( $> 3$   $\mu\text{m}$ ) up to very highly elongated  
323 tubules ( $> 30$   $\mu\text{m}$ ) (mean length,  $8.73 \pm 9.2$   $\mu\text{m}$ ) (**Fig. 1E**). As expected with a defect in division, the  
324 peroxisome number was reduced in MFF-deficient fibroblasts in contrast to controls (mean number,  
325 control fibroblasts:  $244 \pm 116$ , dMFF:  $34 \pm 25$ ) (**Fig. 1F**). Overall, we reveal that peroxisomes in MFF-  
326 deficient patient fibroblasts are fewer and consist of two continuous membrane domains: a spherical  
327 peroxisome body with typical peroxisome size, and a thin, highly elongated tubular structure protruding  
328 from this body.



329

330 **Figure 1.** Morphological characteristics of peroxisomes in MFF-deficient patient fibroblasts are altered.  
 331 (A) Control fibroblasts (C109) and MFF-deficient patient fibroblasts [mutations Q64\* (Shamseldin et  
 332 al. 2012), L62Pfs\*13+R298\* (Koch et al. 2016) and E153Afs\*5 (Koch et al. 2016)] were processed for  
 333 immunofluorescence microscopy using antibodies directed to PEX14, a peroxisomal membrane marker.  
 334 Higher magnification of boxed region is shown. Arrowheads highlight potential membrane  
 335 constrictions. Scale bars, 10  $\mu$ m; magnification, 5  $\mu$ m. (B) Electron micrographs of peroxisomes in  
 336 MFF-deficient cells (MFF<sup>Q64\*</sup>). White arrowheads highlight peroxisomal membrane tubules, black  
 337 arrowheads indicate microtubules. Scale bars, 0.2  $\mu$ m. (C) Confocal (Airyscan) images of peroxisomal  
 338 membrane tubules (anti-PEX14) in MFF<sup>Q64\*</sup> cells co-stained with anti- $\alpha$ -tubulin. White arrowheads

339 indicated co-localisation of peroxisomes and microtubules. Scale bars, 3  $\mu\text{m}$ . **(D)** Measurement of  
 340 peroxisomal width (nm) of bodies and tubules based on electron micrographs of MFF<sup>Q64\*</sup> fibroblasts [n  
 341 = 33 (bodies), 79 (tubules)]. **(E)** Measurement of peroxisomal length ( $\mu\text{m}$ ) from immunofluorescence  
 342 images of MFF<sup>Q64\*</sup> patient fibroblasts (n = 392). **(F)** Quantification of peroxisome number based on  
 343 immunofluorescence images of control (C109) and MFF<sup>Q64\*</sup> fibroblasts (n = 24). Data are from at least  
 344 3 independent experiments. \*\*\*,  $p < 0.001$ ; two-tailed, unpaired t test.

### 345 **3.2. MFF deficiency does not alter standard biochemical parameters associated with** 346 **peroxisomal dysfunction**

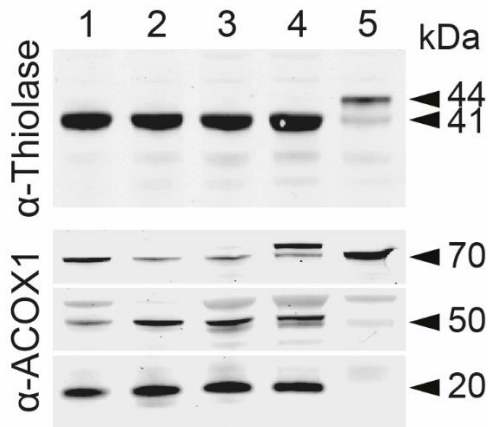
347 Several biochemical parameters were studied to investigate peroxisomal function in cultured fibroblasts  
 348 (**Table 1**). Peroxisomal  $\alpha$ - and  $\beta$ -oxidation activities were measured with different radiolabelled  
 349 substrates, i.e. [<sup>14</sup>C]-phytanic acid, pristanic acid and cerotic acid (C26:0). In addition, very long-chain  
 350 fatty acid (VLCFA) metabolism was studied with a three day D3-C22 loading test, and total VLCFA  
 351 levels and C26-lysophosphatidylcholine levels were determined in cell pellets (Ferdinandusse et al.  
 352 2016). No notable abnormalities were found in all three MFF-deficient cell lines providing no indication  
 353 of a disturbed metabolism of VLCFAs or branched-chain fatty acids in peroxisomes.  $\alpha$ -oxidation values  
 354 were slightly higher than the reference range, but this does not indicate any dysfunction. The activity  
 355 of dihydroxyacetone phosphate acyltransferase (DHAPAT), the first enzyme of the plasmalogen  
 356 biosynthesis pathway located in peroxisomes, was within reference range. The intra-peroxisomal  
 357 processing of the peroxisomal  $\beta$ -oxidation enzymes acyl-CoA oxidase 1 (ACOX1) and 3-ketoacyl-CoA  
 358 thiolase was not altered, suggesting normal peroxisomal matrix protein import and processing activity  
 359 in contrast to fibroblasts from a patient with a peroxisomal biogenesis disorder (**Fig. 2**). This is in line  
 360 with metabolic and biochemical analyses of plasma from different MFF patients (Shamseldin et al. 2012;  
 361 Koch et al. 2016; Nasca et al. 2018). We can confirm from these studies that MFF deficiency does not  
 362 cause alterations to overall peroxisomal biochemical function. This is also in line with reports from  
 363 other disorders affecting the dynamics and plasticity of peroxisomes (e.g. DRP1- or PEX11 $\beta$ -deficiency)  
 364 (Waterham et al. 2007; Ebberink et al. 2012).

	MFF <sup>L62Pfs*13+R298*</sup>	MFF <sup>E153Afs*5</sup>	MFF <sup>Q64*</sup>	Reference range
<b>VLCFAs</b> ( $\mu\text{mol/g}$ protein)				
C26:0	0.30	0.33	0.29	0.16-0.41
C26/C22 ratio	0.06	0.07	0.07	0.03-0.1
<b>C26-lysoPC</b> (pmol/mg protein)	12.3	9.2	7.0	2-14
<b>Alpha-oxidation activity</b> (pmol/(hour.mg protein))	135	104	n.d.	28-95
<b>Beta-oxidation activity</b> (pmol/(hour.mg protein))				
C26:0	2109	1505	n.d.	800-2040
Pristanic acid	1072	1099	n.d.	790-1072
<b>D3C22 loading test</b> ( $\mu\text{mol/g}$ protein)				
D3C26 (chain elongation)	0.29	0.3	0.26	0.16-0.66
D3C16/D3C22 ratio (beta-oxidation)	1.25	1.74	2.27	0.64-2.13
<b>DHAPAT activity</b> (nmol/(2hour.mg protein))	9.2	7.1	6.6	5.9-15.5

365

366 **Table 1.** Biochemical parameters associated with peroxisomal dysfunction are normal in MFF-deficient  
 367 patient fibroblasts. Peroxisomal parameters determined in three MFF-deficient patient fibroblast cell

368 lines MFF<sup>L62Pfs\*13+R298\*</sup> (Koch et al. 2016), MFF<sup>E153Afs\*5</sup> (Koch et al. 2016), and MFF<sup>Q64\*</sup> (Shamseldin et  
369 al. 2012). Very long-chain fatty acid (VLCFA) levels, C26-lysophosphatidylcholine (C26-lysoPC),  $\alpha$ -  
370 and  $\beta$ -oxidation activity, VLCFA metabolism (D3C22 loading test) and dihydroxyacetone phosphate  
371 acyltransferase (DHAPAT) activity were measured. A reference range of control fibroblasts from  
372 healthy individuals is shown for comparison. Data present mean of duplicate measurements. n.d., not  
373 determined; VLCFA, very long-chain fatty acid; C26-lysoPC, C26-lysophosphatidylcholine; DHAPAT,  
374 dihydroxyacetone phosphate acyltransferase.



375

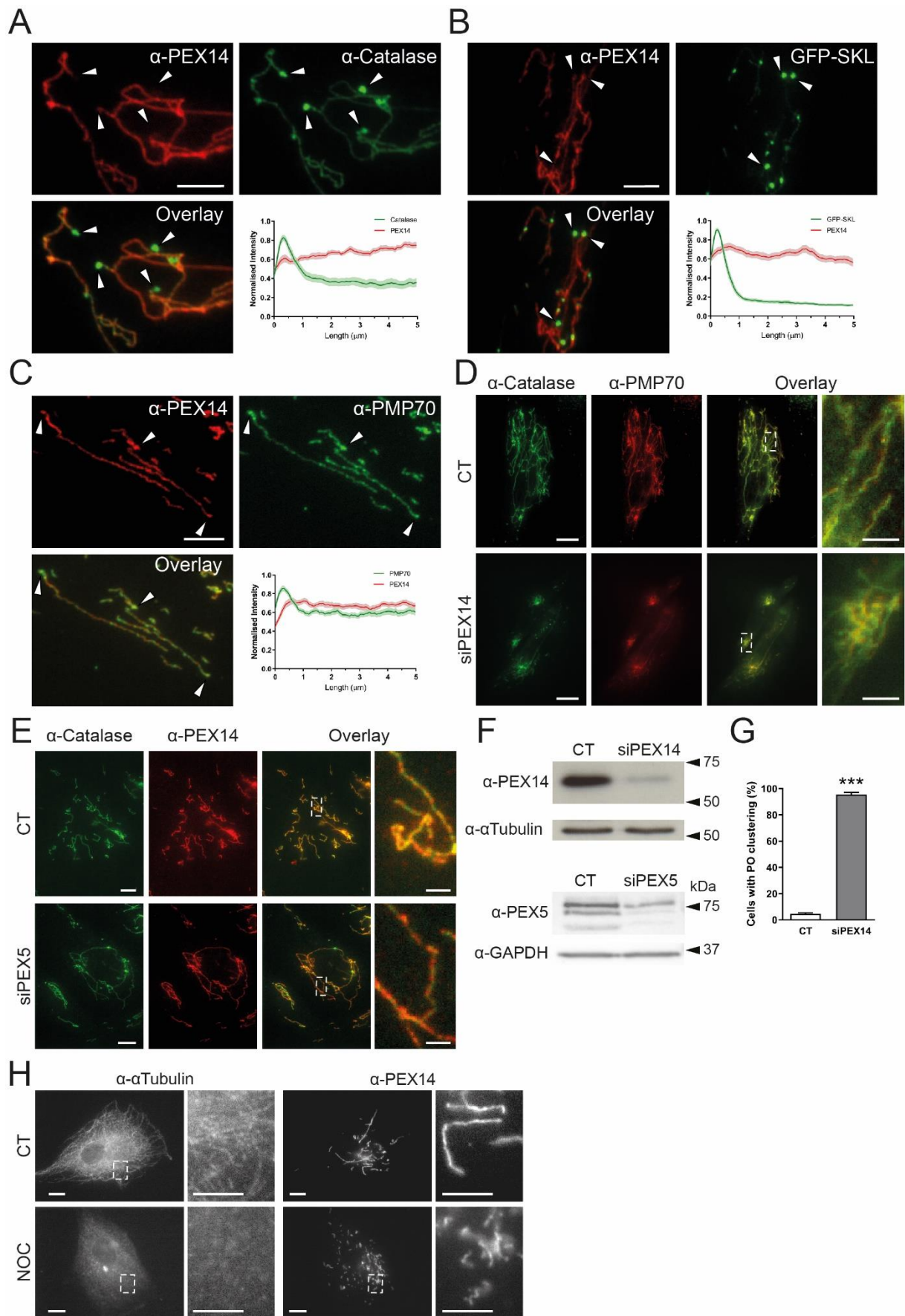
376 **Figure 2.** Immunoblot analysis of fibroblast homogenates from MFF-deficient patients. Antibodies  
377 were directed against peroxisomal 3-ketoacyl-CoA thiolase (upper panel) or peroxisomal acyl-CoA  
378 oxidase 1 (ACOX1; lower panel). Lanes 1-3, MFF-deficient patient fibroblasts MFF<sup>Q64\*</sup> (Shamseldin  
379 et al. 2012), MFF<sup>L62Pfs\*13+R298\*</sup> (Koch et al. 2016) and MFF<sup>E153Afs\*5</sup> (Koch et al. 2016), respectively. Lane  
380 4: control subject, Lane 5: fibroblasts of a patient with Zellweger Spectrum Disorder (ZSD). Results  
381 show normal proteolytic processing of 3-ketoacyl-CoA thiolase (40-kDa) and ACOX1 (50- and 20-kDa)  
382 in the MFF-deficient cell lines, whereas in the ZSD line the unprocessed bands of 3-ketoacyl-CoA  
383 thiolase (44-kDa) and ACOX1 (70-kDa) are present. Note that the protein band above the 70 kDa band  
384 of ACOX1 is non-specific.

### 385 3.3. Protein import into MFF-deficient peroxisomes is impaired in tubular extensions

386 As globular peroxisomal bodies were visible in ultrastructural studies (**Fig. 1B**) but surprisingly less  
387 visible in immunofluorescence studies with anti-PEX14, which labelled predominantly tubular  
388 structures (**Fig. 1A**), we performed co-localisation studies with anti-catalase, a prominent peroxisomal  
389 marker enzyme in the peroxisomal matrix (**Fig. 3A**). In contrast to PEX14, endogenous catalase was  
390 found to localise primarily to the spherical peroxisome bodies, with weaker fluorescence intensity along  
391 the peroxisomal tubules (**Fig. 3A**). Analysis of fluorescence intensity along single peroxisomes of both  
392 PEX14 and catalase confirmed PEX14 fluorescence primarily along tubules with some localisation in  
393 bodies, whereas catalase fluorescence was primarily detected in the peroxisomal body, with reduced  
394 intensity along the tubule (**Fig. 3A**). Peroxisomes import matrix proteins from the cytosol via dedicated  
395 import machinery at the peroxisomal membrane (Francisco et al. 2017). Matrix proteins such as catalase  
396 are imported into peroxisomes via a C-terminal peroxisomal targeting signal (PTS1). These steady-state  
397 observations imply that catalase is mainly imported into the spherical bodies, suggesting that those  
398 represent mature, import-competent structures. To test this hypothesis, we expressed a GFP-fusion  
399 protein with a C-terminal PTS1 signal SKL (GFP-SKL) in MFF-deficient cells. Cells were processed  
400 for immunofluorescence after 24 hours and labelled with anti-PEX14 antibodies (**Fig. 3B**). Similar to  
401 endogenous catalase, exogenously expressed GFP-SKL localised primarily to peroxisomal bodies, with

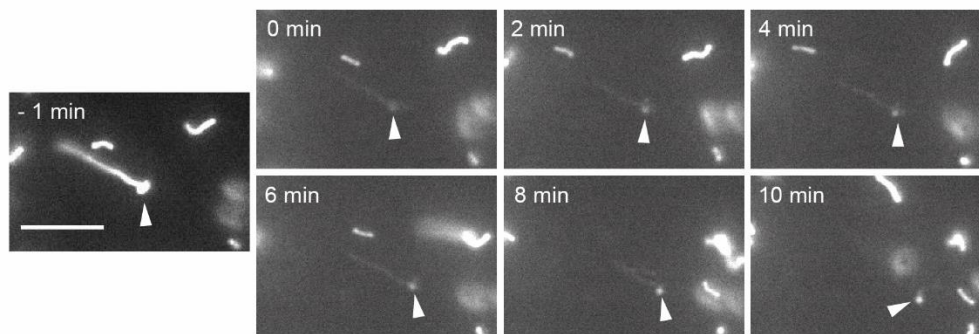
402 less presence in the peroxisomal tubules (**Fig. 3B**). This was confirmed by analysis of fluorescence  
403 intensity (**Fig. 3B**). Immunofluorescence microscopy with the peroxisomal membrane markers PMP70  
404 and PEX14 revealed co-localisation of both membrane proteins at membrane tubules (**Fig. 3C**). PMP70  
405 also localised to the spherical bodies, where PEX14 is less prominent (**Fig. 3C**). These findings indicate  
406 that the spherical bodies represent mature, import-competent peroxisomes, whereas the tubular  
407 extensions comprise a pre-peroxisomal membrane compartment which has not yet fully acquired import  
408 competence for matrix proteins or lacks the capability to retain them. To confirm these conclusions, we  
409 performed FRAP experiments (**Suppl. Fig. S2**). Peroxisomes in MFF-deficient fibroblasts expressing  
410 GFP-SKL were photobleached followed by immediate observation through live-cell imaging. After  
411 photobleaching of the entire organelle (peroxisome body and short tubule), recovery of GFP-SKL  
412 fluorescence was first observed in the peroxisome body, indicating that recovery is due to import of  
413 GFP-SKL into the peroxisome body rather than into the tubule (**Suppl. Fig. S2**). We cannot completely  
414 exclude that there is some matrix protein import into the tubule, which may be slow or less efficient.  
415 However, our findings support our conclusion that spherical bodies are mature import competent  
416 structures, whereas the tubules represent pre-peroxisomal membrane structures which have not yet fully  
417 acquired import competence for matrix proteins or lack the capability to retain them.



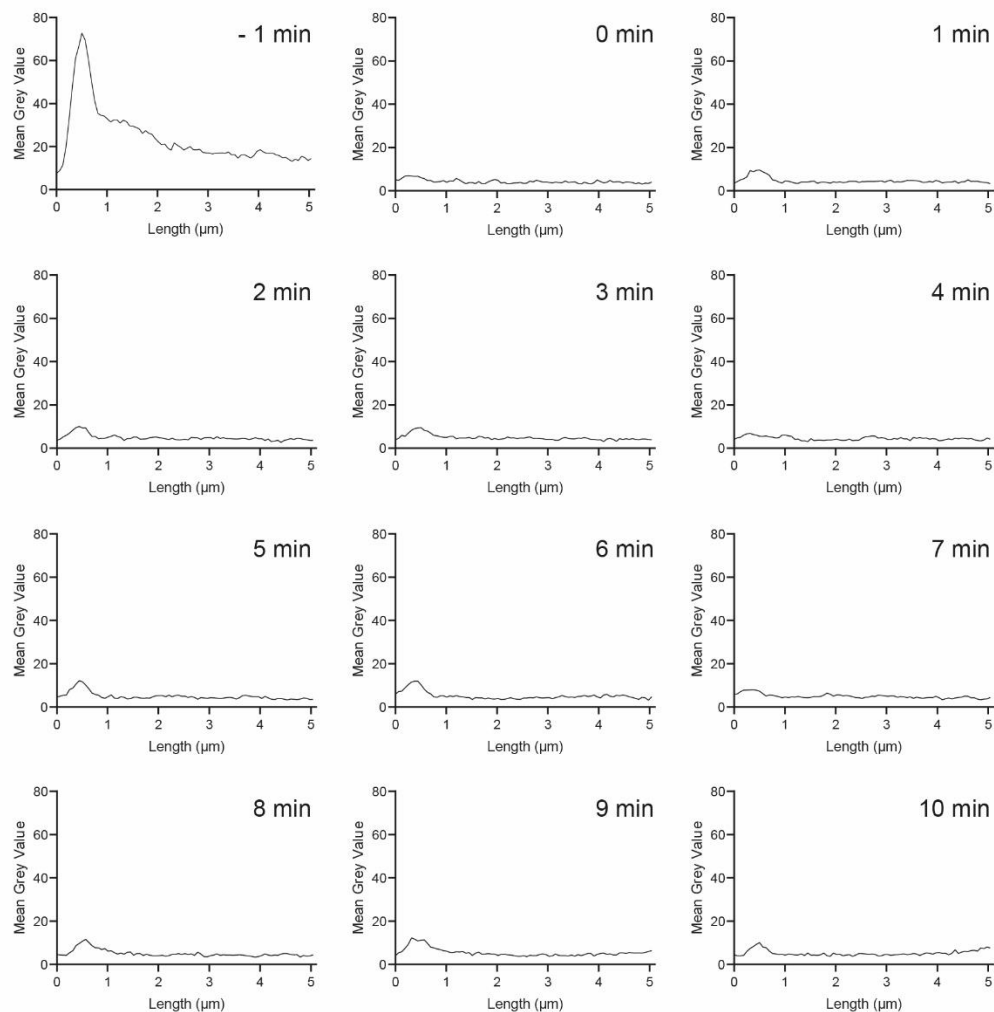


419 **Figure 3.** Altered marker protein distribution in MFF-deficient patient fibroblasts (MFF<sup>Q64\*</sup>). **(A)**  
420 Patient fibroblasts were processed for immunofluorescence microscopy using antibodies against  
421 peroxisomal membrane marker PEX14 and matrix marker catalase, and fluorescence intensity measured  
422 along 5  $\mu\text{m}$  of peroxisome, starting at peroxisome bodies (arrowheads) normalised to the maximum  
423 intensity. Shaded area in graphs represents the standard error of the mean (line) ( $n = 30$ ). Arrowheads  
424 highlight peroxisomal bodies. Scale bar, 5  $\mu\text{m}$ . **(B)** Patient fibroblasts were transfected with a plasmid  
425 encoding EGFP-SKL and processed for immunofluorescence microscopy using an antibody against  
426 PEX14. Quantification was performed as in **A** ( $n = 30$ ). **(C)** As in **A**, using antibodies against membrane  
427 markers PEX14 and PMP70. Quantification was performed as in **A**, **B** ( $n = 30$ ). Scale bar, 5  $\mu\text{m}$ . **(D)**  
428 MFF<sup>Q64\*</sup> fibroblasts were transfected with control siRNA (CT) or PEX14 siRNA (siPEX14) and  
429 processed for immunofluorescence microscopy after 48 hours using antibodies against catalase and  
430 PMP70. Scale bars, 10  $\mu\text{m}$ , magnification, 2  $\mu\text{m}$ . **(E)** As in **D**, transfecting with control siRNA (CT),  
431 or PEX5 siRNA (siPEX5), and processing for immunofluorescence using antibodies against catalase  
432 and PEX14. Scale bars, 10  $\mu\text{m}$ , magnification, 2  $\mu\text{m}$ . **(F)** Immunoblotting of control (CT), PEX14  
433 (siPEX14) or PEX5 siRNA (siPEX5) transfected patient fibroblasts, using antibodies against PEX14,  
434 PEX5 and  $\alpha$ -tubulin or GAPDH (loading control). **(G)** Quantification of peroxisomal clustering in  
435 MFF-deficient fibroblasts either transfected with control (CT) or PEX14 siRNA (siPEX14) ( $n = 150$ ).  
436 Data are from at least 3 independent experiments. \*\*\*,  $p < 0.001$ ; two-tailed, unpaired t test. **(H)**  
437 MFF<sup>Q64\*</sup> patient fibroblasts were treated with 0.07% DMSO (CT), or 10  $\mu\text{M}$  nocodazole (NOC) for four  
438 hours prior to processing for immunofluorescence microscopy using antibodies against  $\alpha$ -tubulin and  
439 PEX14. Scale bars, 10  $\mu\text{m}$ , magnification, 2  $\mu\text{m}$ .

A



B



440

441 **Suppl. Figure S2.** The peroxisomal body is import-competent. MFF-deficient fibroblasts were  
442 transfected with GFP-SKL and grown on 3.5-cm glass bottom dishes. Photo-bleaching experiments  
443 were performed after 24-48 hours using a Visitron 2D FRAP system. The entire organelle (peroxisome  
444 body and short tubule) was photo-bleached (0 min) and recovery of GFP-SKL fluorescence monitored  
445 over a period of 10 minutes (A). Note that GFP-SKL fluorescence was observed in the peroxisome body  
446 (arrowheads), but not in the peroxisome tubule, indicating that recovery is due to import of GFP-SKL  
447 into the peroxisome body. (B) Quantification of fluorescence intensity. Data are presented at the mean  
448 grey value for each increment along the length of the peroxisome. Scale bar, 5  $\mu\text{m}$ .

449

### 450 **3.4. A role of PEX14 in maintaining peroxisomal tubule stability**

451 As PEX14 is part of the matrix protein import machinery (Brown and Baker 2008), its predominant  
452 localisation to the peroxisomal membrane tubules (rather than the import-competent spherical bodies)  
453 is unexpected. However, additional functions for PEX14 have been suggested. Peroxisomes interact  
454 with and move along microtubules (Thiemann et al. 2000; Schrader et al. 2003; Castro et al. 2018). The  
455 N-terminal domain of PEX14 (1-78) has previously been shown to bind tubulin (Bharti et al. 2011;  
456 Theiss et al. 2012). Although PEX14 is not essential for microtubule-dependent peroxisomal motility  
457 (Castro et al. 2018), it may function as a peroxisomal microtubule docking factor. Indeed, in  
458 ultrastructural and confocal studies microtubules were frequently observed in close association with the  
459 entire length of peroxisomal tubules in MFF patient cells (**Fig. 1B, C**). Furthermore, in a previous study,  
460 we showed that highly elongated peroxisomal tubules in fibroblasts are associated with microtubules,  
461 and that tubule elongation is reduced in PEX14-deficient cells (Castro et al. 2018). Based on these  
462 observations, we hypothesised that PEX14 may be required for the stabilisation of highly elongated  
463 peroxisomal tubules. To test this, we depleted PEX14 by siRNA-mediated knock down in MFF-  
464 deficient cells (**Fig. 3D, F, G**). Peroxisomal tubules in these cells are typically stretched out in the cell,  
465 allowing for easy visualisation. However, when PEX14 was knocked down, peroxisomes lost their  
466 tubular morphology and appeared clustered or fragmented (**Fig. 3D**) (cells with clustered/fragmented  
467 morphology: control siRNA:  $4.7 \pm 1.2\%$ , PEX14 siRNA:  $95.3 \pm 3.1\%$ ) (**Fig. 3G**). The peculiar  
468 peroxisome morphology was specific for silencing of PEX14, and was not observed after silencing of  
469 PEX5, excluding an effect of impaired peroxisomal import (**Fig. 3E**). Furthermore, peroxisome  
470 morphology was not altered after silencing of PEX11 $\beta$  or ACBD5 in MFF-deficient cells (Costello et  
471 al. 2017b). Clustering and fragmentation of elongated peroxisomes in MFF-deficient cells was also  
472 observed after depolymerisation of microtubules with nocodazole (**Fig. 3H**). These observations  
473 suggest a role for PEX14 in facilitating and stabilising peroxisomal membrane extensions by linking  
474 the peroxisomal membrane to microtubules. This may explain why PEX14 is predominantly localising  
475 to the highly elongated peroxisomal membranes in MFF patient cells.

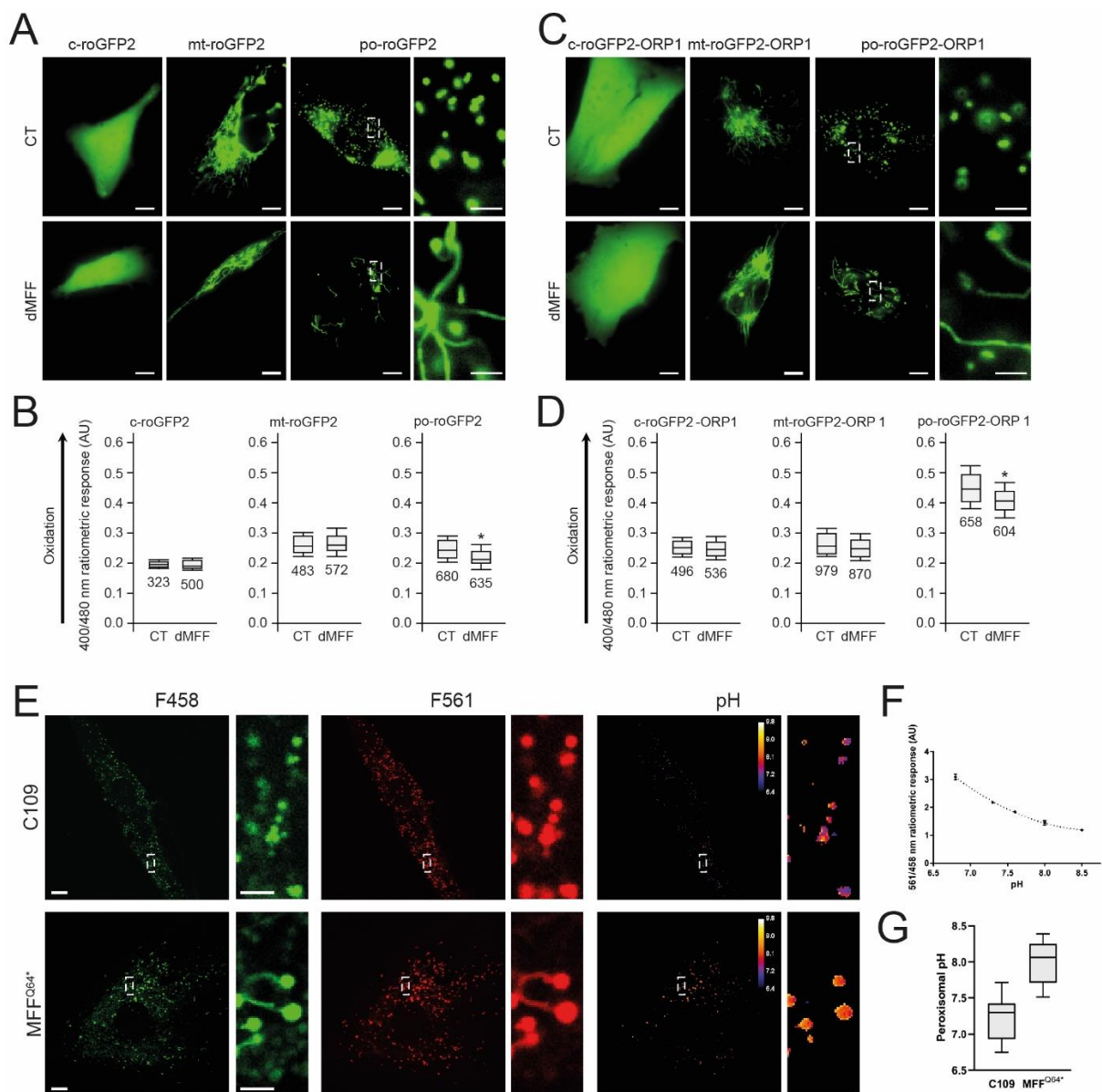
### 476 **3.5. Peroxisomal redox state and pH levels are altered in MFF-deficient fibroblasts**

477 The metabolic parameters of peroxisomes in MFF-deficient cells were normal, in particular their  
478 different functions in lipid metabolism (**Table 1**). As peroxisomes play a role in cellular H<sub>2</sub>O<sub>2</sub>  
479 metabolism and redox homeostasis, we also investigated these parameters (**Fig. 4**). Firstly, we assessed  
480 the glutathione disulphide (GSSG) to glutathione (GSH) ratio, a marker of oxidative balance. Therefore,  
481 MFF-deficient SV40 large T antigen-transformed human fibroblasts (HUFs-T) were transfected with a  
482 plasmid encoding cytosolic, mitochondrial or peroxisome-targeted roGFP2 (**Fig. 4A**). RoGFP2 is a  
483 highly responsive, pH-independent sensor for the glutathione redox couple, and oxidation causes a shift  
484 of its excitation maximum from 488 nm to 405 nm (Ivashchenko et al. 2011; Lismont et al. 2017).  
485 Analyses of the 400/480 ratiometric responses of peroxisome-targeted roGFP2 revealed that the intra-  
486 peroxisomal pool of glutathione is less oxidized in the MFF-deficient fibroblasts than in the control  
487 cells (**Fig. 4B**). In contrast, no alterations in the glutathione redox state could be detected in the cytosol  
488 or the mitochondrial matrix.

489 To monitor changes in hydrogen peroxide homeostasis, MFF-deficient HUFs-T and controls were  
490 transfected with plasmids coding for cytosolic, mitochondrial, or peroxisome-targeted roGFP2-ORP1,  
491 a H<sub>2</sub>O<sub>2</sub>-responsive variant of roGFP2 (**Fig. 4C**) (Lismont et al. 2019b). No changes in oxidation state  
492 were observed in the cytosol and mitochondria (**Fig. 4D**). However, for peroxisomes, a decreased  
493 400/480 nm ratiometric response was seen (**Fig. 4D**), indicating reduced levels of H<sub>2</sub>O<sub>2</sub> inside  
494 peroxisomes in MFF-deficient cells.

495 In addition, we used peroxisome-targeted pHRed (pHRed-PO), another ratiometric probe, to assess  
 496 peroxisomal pH in MFF-deficient patient fibroblasts (Tantama et al. 2011; Godinho and Schrader 2017).  
 497 Importantly, this sensor is insensitive to changes in H<sub>2</sub>O<sub>2</sub> levels (Tantama et al. 2011). The pHRed-PO  
 498 probe successfully targets to peroxisomes in control and MFF-deficient fibroblasts (**Fig. 4E**). It mainly  
 499 distributes to the import-competent spherical peroxisomal bodies, but also to the membrane tubules  
 500 (**Fig. 4E**). Following calibration of the pHRed probe (**Fig. 4F**), the intra-peroxisomal pH can be  
 501 calculated based on the 458/561 nm ratiometric response. Interestingly, intra-peroxisomal pH in MFF-  
 502 deficient fibroblasts was found to be more alkaline than in control fibroblasts (**Fig. 4G**) (mean  
 503 peroxisomal pH, control:  $7.24 \pm 0.30$ , patient fibroblasts:  $8.00 \pm 0.29$ ).

504 Overall, these findings point towards alterations in the peroxisomal redox environment. Specifically,  
 505 we observed a decrease in the GSSG/GSH ratio and H<sub>2</sub>O<sub>2</sub> levels in MFF-deficient fibroblasts. In  
 506 addition, we have shown that absence of MFF results in a more alkaline intra-peroxisomal pH. This  
 507 suggests that MFF-deficiency may compromise normal peroxisomal redox regulation.



509 **Figure 4.** Peroxisomal redox state and pH levels are altered in MFF-deficient fibroblasts. Control (CT)  
510 or MFF-deficient (dMFF) SV40 large T antigen-transformed human fibroblasts (HUFs-T) were  
511 transfected with a plasmid encoding cytosolic (c-), mitochondrial (mt-) or peroxisomal (po-) roGFP2  
512 (**A, B**) or roGFP2-ORP1 (**C, D**). (**A**) Distribution patterns of the respective roGFP2 proteins. Higher  
513 magnification view of po-roGFP2 is shown. (**B**) Box plot representations of the 400/480 nm  
514 fluorescence response ratios of the respective roGFP2 proteins. (**C**) Distribution patterns of the  
515 respective roGFP2-ORP1 proteins. Higher magnification view of po-roGFP2-ORP1 is shown. Note that  
516 high expression levels of the peroxisomal reporter proteins result in labelling of peroxisome tubules.  
517 (**D**) Box plot representations of the 400/480 nm fluorescence response ratios of the respective roGFP2  
518 proteins. The bottom and top of each box represent the 25th and 75th percentile values, respectively;  
519 the horizontal line inside each box represents the median; and the horizontal lines below and above each  
520 box denote the mean minus and plus one standard deviation, respectively. The total number of  
521 measurements (two independent experiments; minimum 15 individual measurements in at least 20  
522 randomly chosen cells) is indicated below each box plot. The data from the dMFF cell line were  
523 statistically compared with those from the CT cell line (\*\*,  $p < 0.01$ ). (**E**) Distribution patterns of  
524 pHRed-PO in control (C109) and MFF-deficient patient fibroblasts (MFF<sup>Q64\*</sup>) at excitation wavelengths  
525 of 458 and 561 nm, along with digital visualisation of individual peroxisomal pH levels. Higher  
526 magnification views of boxed regions are indicated. (**F**) Calibration of the pHRed probe using cytosolic  
527 pHRed. The 458/561 ratiometric response is given at each pH level. AU, arbitrary units. (**G**)  
528 Quantification of peroxisomal pH in control (C109) and MFF<sup>Q64\*</sup> cells, converting the ratiometric  
529 response to pH using the calibration curve ( $n = 20$ ). Scale bars, 10  $\mu\text{m}$ ; magnifications, 2  $\mu\text{m}$ . Data are  
530 from at least 2-3 independent experiments. \*,  $p < 0.05$ ; \*\*\*,  $p < 0.001$ ; two-tailed, unpaired t test.

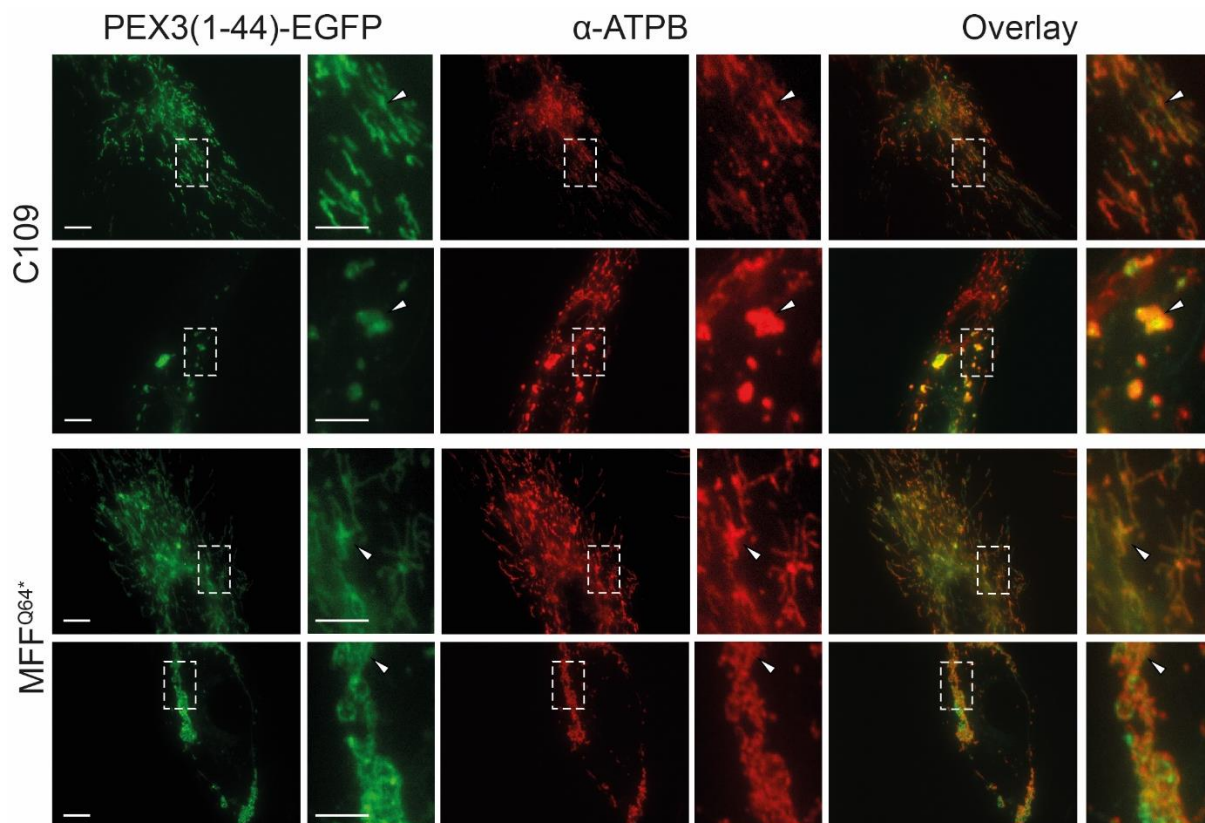
531

### 532 **3.6. Highly elongated peroxisomes in MFF-deficient fibroblasts can be degraded by autophagic** 533 **processes**

534 Autophagic processes are important for the maintenance of cellular homeostasis and the integrity of  
535 organelles (Anding and Baehrecke 2017). Peroxisome homeostasis is achieved via a tightly regulated  
536 interplay between peroxisome biogenesis and degradation via selective autophagy (pexophagy)  
537 (Eberhart and Kovacs 2018). It is still unclear if highly elongated peroxisomes are spared from  
538 pexophagy, e.g. due to physical limitations, as the elongated peroxisomes may not fit into the  
539 autophagosome. Such a scenario would prevent degradation of peroxisomes and could have  
540 pathophysiological consequences.

541 To examine if highly elongated peroxisomes in MFF-deficient fibroblasts can be degraded by  
542 autophagic processes, we first induced pexophagy by the expression of a fragment of peroxisomal  
543 biogenesis protein PEX3. Expression of the first 44 amino acids of the peroxin PEX3, which can insert  
544 into the peroxisome membrane, was observed to cause complete removal of peroxisomes (Soukupova  
545 et al. 1999). When expressing *HsPEX3(1-44)-EGFP* in control fibroblasts (**Fig. 5A, B**), peroxisomes  
546 were greatly reduced in number, with many GFP expressing cells showing almost complete loss of  
547 PEX14 labelling (**Fig. 5A, C109**). As reported earlier, loss of peroxisomes resulted in mistargeting of  
548 *HsPEX3(1-44)-EGFP* to the mitochondria (Soukupova et al. 1999) (**Suppl. Fig. S3**). Interestingly, in  
549 MFF-deficient fibroblasts, expression of *HsPEX3(1-44)-EGFP* also caused a marked reduction of  
550 peroxisomes (**Fig. 5A, middle panel, B**) or complete loss of PEX14 labelling (**Fig. 5A, lower panel,**  
551 **B**). Increased mitochondrial mistargeting of *HsPEX3(1-44)-EGFP* was observed with increased loss of  
552 peroxisomes (**Fig. 5A; Suppl. Fig. S3**).

553



554

555

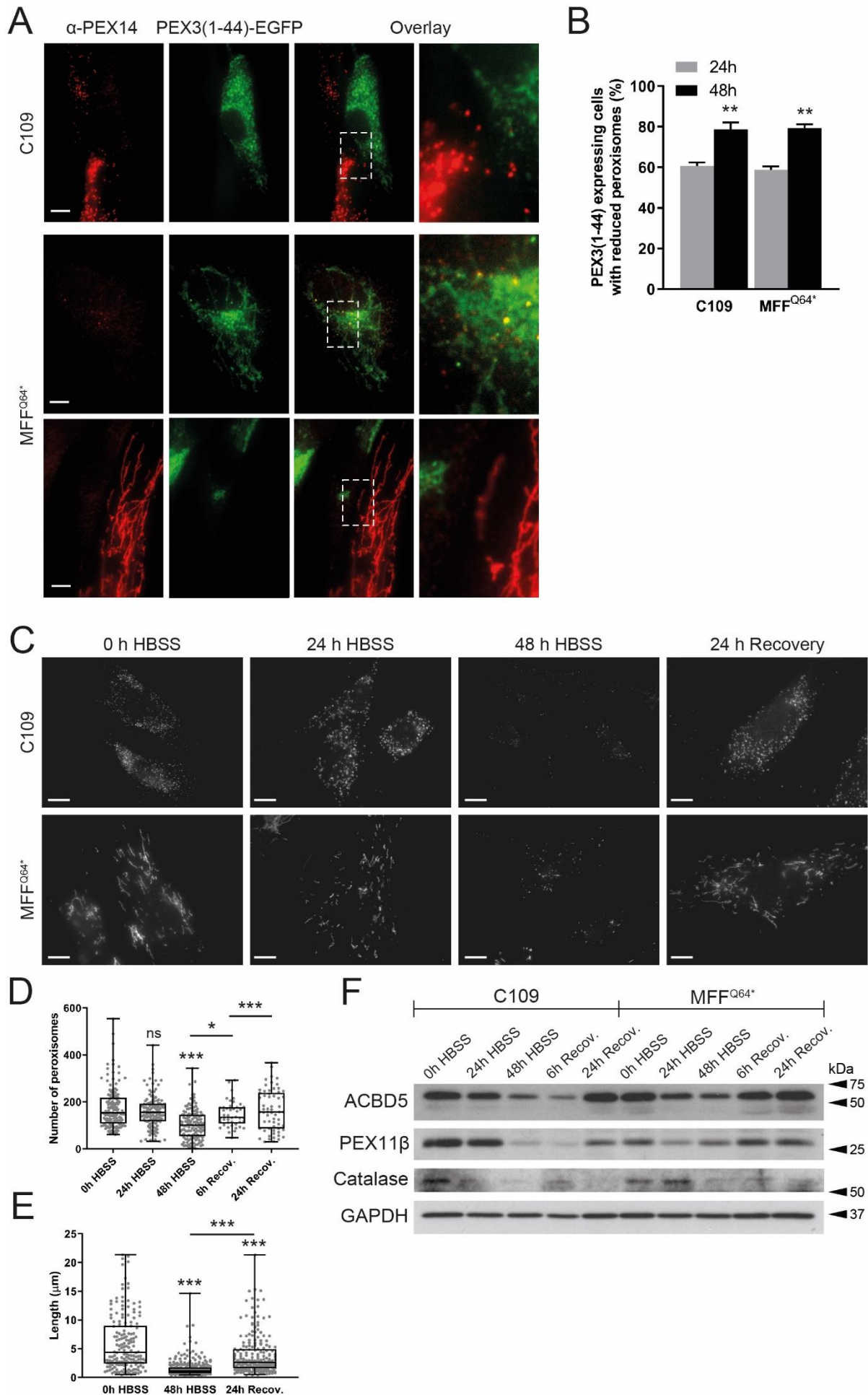
556 **Suppl. Figure S3.** HsPEX3(1-44)-EGFP is targeted to mitochondria when peroxisomes are lost. Human  
557 control (C109) or MFF-deficient (MFF<sup>Q64\*</sup>) fibroblasts were transfected with a plasmid coding for  
558 HsPEX3(1-44)-EGFP to induce peroxisome degradation and processed for immunofluorescence after  
559 24 and 48 hours using antibody against mitochondrial ATP synthase (ATPB). Note the mistargeting of  
560 HsPEX3(1-44)-EGFP to mitochondria (arrowheads). Furthermore, mitochondrial morphology is  
561 altered including fragmentation and clustering. Scale bars, 10  $\mu$ m, magnification, 2  $\mu$ m.

562

563 To examine peroxisome degradation under more physiological conditions, we applied nutrient  
564 deprivation. Limiting amino acids in the growth media of cells has been previously shown to induce  
565 removal of peroxisomes (Sargent et al. 2016). For assessing peroxisome degradation, controls and MFF-  
566 deficient fibroblasts were cultured in Hanks' Balanced Salt Solution (HBSS), which lacks amino acids.  
567 After 0, 24 and 48 hours, cells were processed for immunofluorescence using anti-PEX14 as a  
568 peroxisomal marker (**Fig. 5C**). In control cells, we observed a marked decrease in spherical peroxisomes,  
569 with often only a few organelles remaining after 48 hours in HBSS (**Fig. 5C, D**). As with HsPEX3(1-  
570 44)-EGFP, we also observed a decrease in peroxisomes in nutrient-deprived MFF-deficient cells, which  
571 was accompanied by a significant reduction in peroxisomal length (mean peroxisomal length, 0 hours  
572 HBSS:  $6.08 \pm 4.90 \mu$ m, 48 hours HBSS:  $1.55 \pm 1.43 \mu$ m) (**Fig. 5C, E**). The reduction in peroxisomes  
573 was accompanied by a reduction in peroxisomal marker proteins (**Fig. 5F**). Peroxisomes and protein  
574 levels recovered in control and MFF-deficient cells after switching to complete culture medium for 24  
575 hours (**Fig. 5C-F**). Interestingly, the switch to complete growth medium resulted in the recovery of

576 elongated peroxisomes (mean peroxisomal length, 24 hours recovery:  $3.84 \pm 3.40 \mu\text{m}$ ) (**Fig. 5E**),  
577 indicating that peroxisomes in MFF-deficient fibroblasts are still dynamic under certain conditions.  
578 Overall, these data show that highly elongated peroxisomes in MFF-deficient cells are not spared from  
579 autophagic processes and are capable of being degraded.





581 **Figure 5.** Degradation of peroxisomes in MFF-deficient patient fibroblasts. **(A)** Human control (C109)  
582 or MFF-deficient (MFF<sup>Q64\*</sup>) fibroblasts were transfected with a plasmid coding for *HsPEX3*(1-44)-  
583 EGFP to induce peroxisome degradation and processed for immunofluorescence after 24 and 48 hours  
584 using antibodies against PEX14. Note the almost complete loss of PEX14, and mistargeting of  
585 *HsPEX3*(1-44)-EGFP to mitochondria when peroxisomes are lost (Soukupova et al. 1999) (**Suppl. Fig.**  
586 **S3**). Scale bars, 10  $\mu$ m. magnification, 2  $\mu$ m **(B)** Quantification of *HsPEX3*(1-44)-EGFP expressing  
587 cells (control fibroblasts, C109; MFF-deficient, MFF<sup>Q64\*</sup>) showing reduced peroxisomes after 24 and  
588 48 hours (n = 150).. \*\*\*,  $p < 0.001$ ; two-tailed, unpaired t test. **(C)** Human control (C109) and MFF-  
589 deficient fibroblasts (MFF<sup>Q64\*</sup>) were incubated in Hanks' Balanced Salt Solution (HBSS) to induce  
590 peroxisome degradation and processed for immunofluorescence after 0, 24 and 48 hours and after 24  
591 hours recovery in complete culture medium using antibodies against PEX14. Scale bars, 10  $\mu$ m. **(D)**  
592 Quantification of the number of peroxisomes in C109 control fibroblasts following incubation in HBSS  
593 and recovery in complete culture medium (see **C**) [n = 62 (24h Recovery) to 139 (48h HBSS)]. \*\*\*,  $p$   
594  $< 0.001$ , \*,  $p < 0.1$ , ns, not significant, Ordinary one-way ANOVA with Tukey's multiple comparisons  
595 test. **(E)** Quantification of peroxisome length in MFF<sup>Q64\*</sup> fibroblasts following 0, 48 hours of HBSS  
596 treatment, and after 24 hours of recovery in complete culture medium [n = 167 (0h HBSS) to 297 (48h  
597 HBSS)]. Data are from at least 3 independent experiments. \*\*\*,  $p < 0.001$ , Ordinary one-way ANOVA  
598 with Tukey's multiple comparisons test. **(F)** Immunoblot of cell lysates from control (C109) and MFF-  
599 deficient fibroblasts (MFF<sup>Q64\*</sup>) which were incubated in HBSS for 0, 24, and 48 hours, and after 6 and  
600 24 hours of recovery in complete culture medium. Antibodies against the peroxisomal membrane  
601 proteins ACBD5, PEX11 $\beta$  and Catalase were applied. Anti-GAPDH was used as a loading control.  
602 Equal amounts of protein were loaded. Molecular mass markers (kDa) are indicated on the right.

## 603 4. Discussion

604 Whereas dysfunctional peroxisome metabolism and associated diseases are generally well studied, the  
605 consequences and pathophysiology caused by specific disruption to peroxisome dynamics and plasticity  
606 are less clear. Mutations in DRP1, MFF or PEX11 $\beta$  have been linked to defects in the membrane  
607 dynamics and division of peroxisomes rather than to loss of metabolic functions (Waterham et al. 2007;  
608 Shamseldin et al. 2012; Ebberink et al. 2012; Koch et al. 2016; Taylor et al. 2017; Nasca et al. 2018).  
609 This is in contrast to the classical peroxisome biogenesis disorders (e.g. Zellweger spectrum disorders)  
610 or single enzyme deficiencies and can complicate diagnosis through metabolic biomarkers. Despite  
611 considerable progress in the field, the precise molecular functions of several of the proteins regulating  
612 peroxisomal plasticity remain to be determined as well as the contribution of impaired peroxisomal  
613 dynamics to the pathophysiology of the above disorders. In line with this, depletion of PEX11 $\beta$  in  
614 epidermal cells was recently reported to result in abnormal mitosis and organelle inheritance, thus  
615 affecting cell fate decisions (Asare et al. 2017). As DRP1 and MFF also localise to mitochondria, and  
616 as loss of DRP1 or MFF function also inhibits mitochondrial division, focus has so far mainly been on  
617 mitochondrial properties under those conditions. Here, we assessed the extent to which peroxisomal  
618 functions and properties are altered in MFF-deficient cells.

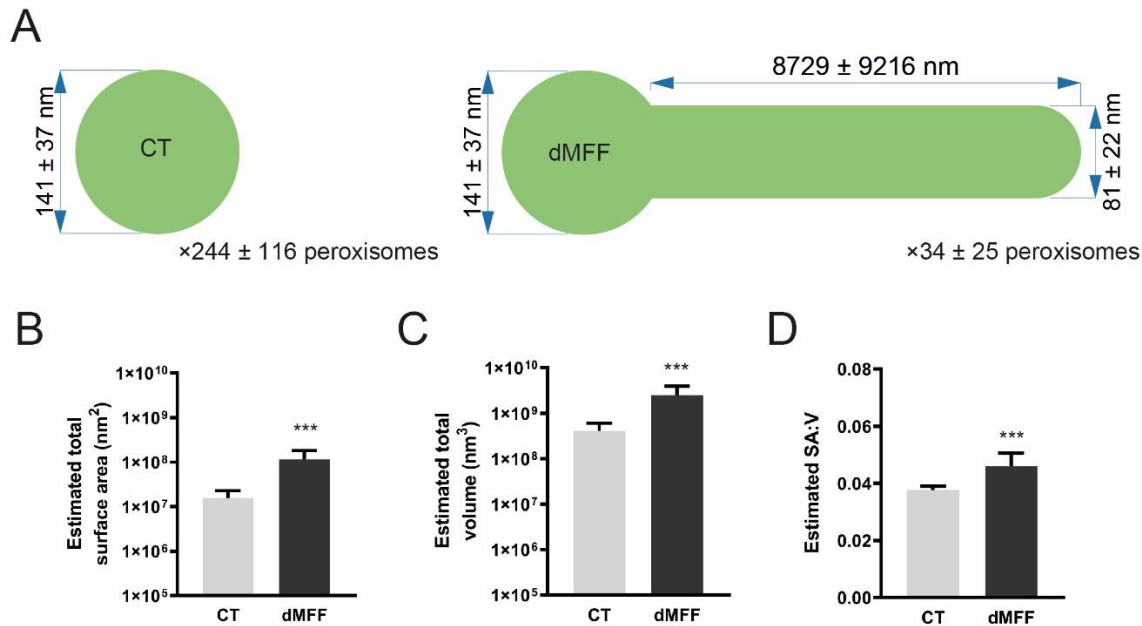
619 There are currently six patients with MFF-deficiency identified, with various mutations in the MFF  
620 protein shown; c.C190T:p.Q64\* (Shamseldin et al. 2012); c.184dup:p.L62Pfs\*13 combined with  
621 c.C892T:p.R298\* (Koch et al. 2016); c.453\_454del:p.E153Afs\*5 (Koch et al. 2016); and most recently  
622 c.C892T:p.R298\* alone (Nasca et al. 2018). Patient skin fibroblasts show a loss of MFF function with  
623 mitochondrial and peroxisomal hyper-elongation, and the patients themselves present with neurological  
624 abnormalities, showing developmental delay, peripheral neuropathy, optic atrophy, and Leigh-like  
625 encephalopathy (Shamseldin et al. 2012; Koch et al. 2016; Nasca et al. 2018). We confirmed a similar  
626 degree of peroxisomal hyper-elongation in skin fibroblasts from three different, previously  
627 characterized patients suffering from MFF-deficiency when maintained under the same culture  
628 conditions [c.C190T:p.Q64\* (Shamseldin et al. 2012); c.184dup:p.L62Pfs\*13 combined with  
629 c.C892T:p.R298\* (Koch et al. 2016); c.453\_454del:p.E153Afs\*5 (Koch et al. 2016)]. Furthermore,  
630 peroxisomal biochemical parameters related to fatty acid  $\alpha$ - and  $\beta$ -oxidation, plasmalogen biosynthesis,  
631 or matrix protein import/processing did not reveal any deficiencies in fibroblasts from those patients.  
632 This is in agreement with biochemical studies in other MFF-deficient patient fibroblasts (Koch et al.  
633 2016; Nasca et al. 2018). Overall, these findings support the notion that defects in the membrane  
634 dynamics and division of peroxisomes rather than loss of metabolic functions contribute to the disease  
635 pathophysiology.

636 Similar observations in PEX11 $\beta$ - or DRP1-deficient cells (Waterham et al. 2007; Ebberink et al. 2012)  
637 have led to the general assumption that defects in peroxisomal dynamics and division result in elongated  
638 peroxisomes, which are, however, largely functional and otherwise normal. We now reveal in MFF-  
639 deficient cells that this is not the case. We show that the elongated peroxisomes in those cells are  
640 composed of a spherical body, which represents a mature, import-competent peroxisome, and of thin,  
641 tubular extensions, which likely represent pre-peroxisomal membrane compartments; not yet fully  
642 import-competent for peroxisomal matrix proteins. An alternative interpretation may be that the tubular  
643 structures are to some degree import-competent but lack mechanisms to retain the imported matrix  
644 proteins. Such a mechanism for retaining matrix proteins may be provided by membrane constriction,  
645 which is impaired in MFF-deficient cells.

646 These observations are consistent with the proposed multi-step maturation model of peroxisomal  
647 growth and division and with previous data on tubular membrane extensions after expression of

648 PEX11 $\beta$  (Delille et al. 2010; Schrader et al. 2012, 2016). In this respect, elongated peroxisomes in MFF-  
649 deficient cells resemble those observed after expression of a division-incompetent PEX11 $\beta$ , which also  
650 results in elongated peroxisomes with an import-competent spherical body and a pre-peroxisomal  
651 membrane expansion (Delille et al. 2010). In contrast, elongated peroxisomes in DRP1-depleted cells  
652 are constricted, with a “beads-on-a string” like appearance, and the interconnected spherical  
653 peroxisomes (“beads”) are import-competent for matrix proteins (Koch et al. 2004). These constrictions  
654 may therefore provide a mechanism to retain matrix proteins. This indicates that a defect in MFF  
655 influences peroxisome division earlier than a defect in DRP1, and results in a maturation defect of  
656 elongated peroxisomes, which are unable to constrict and to subsequently import and/or retain matrix  
657 proteins. Re-expression of MFF in the MFF-deficient fibroblasts early on results in a spot-like  
658 localization of MFF on elongated peroxisomes indicating a role for MFF in the assembly of the division  
659 machinery. In line with this, it has recently been shown that MFF can act as a sensor but also potentially  
660 as an inducer of mitochondrial constriction (Helle et al. 2017). We propose that MFF deficiency, which  
661 impairs peroxisomal membrane constriction and proper assembly of the division machinery, blocks  
662 further maturation of the pre-peroxisomal membrane compartment.

663 This means that, although the number of fully functional peroxisomes is reduced and matrix proteins  
664 are largely restricted to the mature spherical bodies, membrane surface area and volume of the  
665 peroxisomal compartment are increased in MFF-deficient cells (mean estimated total surface area,  
666 control fibroblasts:  $1.55 \times 10^7 \pm 7.29 \times 10^6$  nm<sup>2</sup>, dMFF:  $1.15 \times 10^8 \pm 6.57 \times 10^8$  nm<sup>2</sup>; mean estimated total  
667 volume, control fibroblasts:  $4.1 \times 10^8 \pm 1.94 \times 10^8$  nm<sup>3</sup>, dMFF  $2.5 \times 10^9 \pm 1.45 \times 10^9$  nm<sup>3</sup>) (**Suppl. Fig. S4**),  
668 as well as the surface area to volume ratio (mean estimated SA:V, control fibroblasts:  $0.038 \pm 0.001$ ,  
669 dMFF:  $0.046 \pm 0.005$ ) (**Suppl. Fig. S4**). This likely explains why biochemical functions of elongated  
670 peroxisomes are overall normal under standard conditions. However, it can be speculated that sudden  
671 environmental changes (e.g. an increase in peroxisomal substrates via nutrients/diet or stress conditions),  
672 which require increased peroxisomal metabolic activity and number, will overwhelm the capacity of  
673 the peroxisomal compartment in MFF-deficient cells. This may also explain why mild alterations of  
674 peroxisomal metabolism are occasionally observed in patients with defects in peroxisomal dynamics  
675 and division (Waterham et al. 2007; Ebberink et al. 2012; Taylor et al. 2017). Furthermore, peroxisomes  
676 in patient cells may be less able to cope with increased expression of peroxisomal matrix enzymes or  
677 PMPs. Those may accumulate in the cytoplasm and may be degraded or mistargeted (e.g. to  
678 mitochondria) due to the reduced number of import-competent peroxisomes (Ebberink et al. 2012).



679

680 **Suppl. Figure S4.** Calculations of peroxisomal surface area, volume, and surface area to volume ratio.  
681 (A) Values used for calculations (mean  $\pm$  SD). For the non-elongated control (CT) body diameter, the  
682 value obtained from measurement of peroxisomal bodies in MFF<sup>Q64\*</sup> was used. (B) Estimated total  
683 peroxisomal surface area in control (CT) and MFF-deficient (dMFF) fibroblasts, based on an average  
684 of a computer-generated population of peroxisomes using values taken from the distributions shown in  
685 A. (C) Estimated total peroxisomal volume, and (D) estimated surface area to volume ratio (SA:V).  
686 Error bars show the mean + SD for 10,000 generated peroxisome populations. \*\*\*,  $p < 0.001$ ; two-  
687 tailed, unpaired t test.

688 We also show that peroxisomal matrix and membrane proteins do not distribute evenly along the  
689 elongated peroxisomes in MFF-deficient cells. Endogenous catalase or exogenously expressed GFP-  
690 SKL predominantly localise to the spherical body, whereas PEX14 localises predominantly to the  
691 tubular membrane extensions. A heterogeneous distribution of peroxisomal proteins during membrane  
692 growth and division has been reported previously (Delille et al. 2010; Capińska et al. 2011). The specific  
693 mechanisms which restrict the mobility of the peroxisomal proteins and keep them within the spherical  
694 or tubular membrane domains are still unknown, but may depend on protein oligomerization and/or a  
695 specific lipid environment. However, the prominent localisation of PEX14, a component of the  
696 docking/translocation complex for matrix protein import, to the tubular peroxisomal membranes in  
697 MFF-deficient cells is unusual. It is possible that PEX14, which has been reported to interact with  
698 microtubules (Bharti et al. 2011; Theiss et al. 2012), may also act as a peroxisome-microtubule docking  
699 factor: it predominantly localises to the peroxisomal membrane extensions in MFF patient cells and  
700 may anchor them to microtubules in order to stabilise those highly elongated, delicate membrane  
701 structures and to facilitate membrane extension. The membrane topology of PEX14 is poorly defined,  
702 but a recent study suggested that the N-terminal domain is protease-protected and may not be exposed  
703 to the cytosol (Barros-Barbosa et al. 2019). Such a topology may be inconsistent with tubulin-binding,  
704 but it is possible that different populations or complexes of PEX14 exist which may fulfil different  
705 functions at the peroxisomal membrane.

706 Peroxisomes are oxidative organelles with important roles in cellular redox homeostasis (Fransen and  
707 Lismont 2018). Alterations in their redox metabolism have been suggested to contribute to aging and

708 the development of chronic diseases such as neurodegeneration, diabetes, and cancer (Fransen and  
709 Lismont 2019). Using genetically encoded fluorescent sensors with ratiometric readout in live-cell  
710 approaches, we revealed alterations in the glutathione redox potential within peroxisomes of MFF-  
711 deficient fibroblasts, which was less oxidising compared to controls. In addition, we detected reduced  
712 levels of peroxisomal H<sub>2</sub>O<sub>2</sub> in these cells. Given that the peroxisomal parameters (**Table 1**) and catalase  
713 levels (**Fig. 5F**) are similar in control and MFF-deficient human fibroblasts, the possible mechanisms  
714 underlying these observations remain a subject of speculation. In this context, it is interesting to note  
715 that in a previous study in which mouse embryonic fibroblasts were cultured in medium containing  
716 1,10-phenanthroline, a Zn<sup>2+</sup>-chelating compound that induces oxidative stress and disrupts peroxisomal  
717 and mitochondrial function (Coyle et al. 2004; Jo et al. 2015), the intra-peroxisomal redox state in  
718 tubular peroxisomal compartments was observed to be slightly lower than in spherical bodies (Lismont  
719 et al. 2017). Given that (i) peroxisome-derived H<sub>2</sub>O<sub>2</sub> can easily cross the peroxisomal membrane  
720 (Lismont et al. 2019a), and (ii) the surface to volume ratio is larger in the tubular structures, this may  
721 be explained by the fact that H<sub>2</sub>O<sub>2</sub> can diffuse faster out of the tubular structures than out of the spherical  
722 bodies. Alternatively, as this study indicates that matrix proteins are predominantly imported into the  
723 spherical bodies and less into the peroxisomal tubules (**Fig. 3; Suppl. Fig. S2**), the lower values for  
724 peroxisomal redox parameters in the tubular structures may also be due to the fact that these structures  
725 contain less H<sub>2</sub>O<sub>2</sub>-producing oxidases. However, in contrast to what was observed before in cells  
726 cultured in the presence of 1,10-phenanthroline, no significant differences in the glutathione redox state  
727 or H<sub>2</sub>O<sub>2</sub> levels could be detected between the spherical and tubular structures in MFF-deficient cells  
728 (data not shown). Importantly, the glutathione redox balance and hydrogen peroxide levels in the  
729 cytosol and mitochondria were similar to controls, indicating peroxisome-specific alterations due to  
730 loss of MFF-function. Peroxisome-derived H<sub>2</sub>O<sub>2</sub> may be an important signalling messenger that  
731 controls cellular processes by modulating protein activity through cysteine oxidation (Fransen and  
732 Lismont 2019). However, the precise interrelationship between peroxisomal redox metabolism, cell  
733 signalling, and human disease remains to be elucidated. Further insight may come from the  
734 identification of primary targets for peroxisome-derived H<sub>2</sub>O<sub>2</sub>. We also revealed changes in the  
735 peroxisomal pH in MFF-deficient fibroblasts, which was more alkaline than in controls. The pI of most  
736 peroxisomal enzymes is basic, and consistent with this, an alkaline pH has been reported for the  
737 peroxisomal lumen (Dansen et al. 2000; van Roermund et al. 2004; Godinho and Schrader 2017).  
738 Studies addressing peroxisomal pH under disease conditions are scarce, but a more acidic peroxisomal  
739 pH has been reported in fibroblasts from patients suffering from Rhizomelic Chondrodysplasia Punctata  
740 type 1, a PBD based on a defect in the import receptor PEX7 and impaired matrix protein import of  
741 PTS2-containing cargo (Dansen et al. 2000). It remains to be determined if those changes are the result  
742 of slightly altered metabolic activity and/or changes in membrane properties which impact on  
743 peroxisomal membrane channels/transporters. In line with this, calcium influx into peroxisomes has  
744 been reported to induce a minor increase of peroxisomal pH (Lasorsa et al. 2008). Whether peroxisomes  
745 possess a proton pump is still debated, but it has been suggested that a peroxisomal proton gradient may  
746 be needed to drive other transport processes across the peroxisomal membrane (Rottensteiner and  
747 Theodoulou 2006).

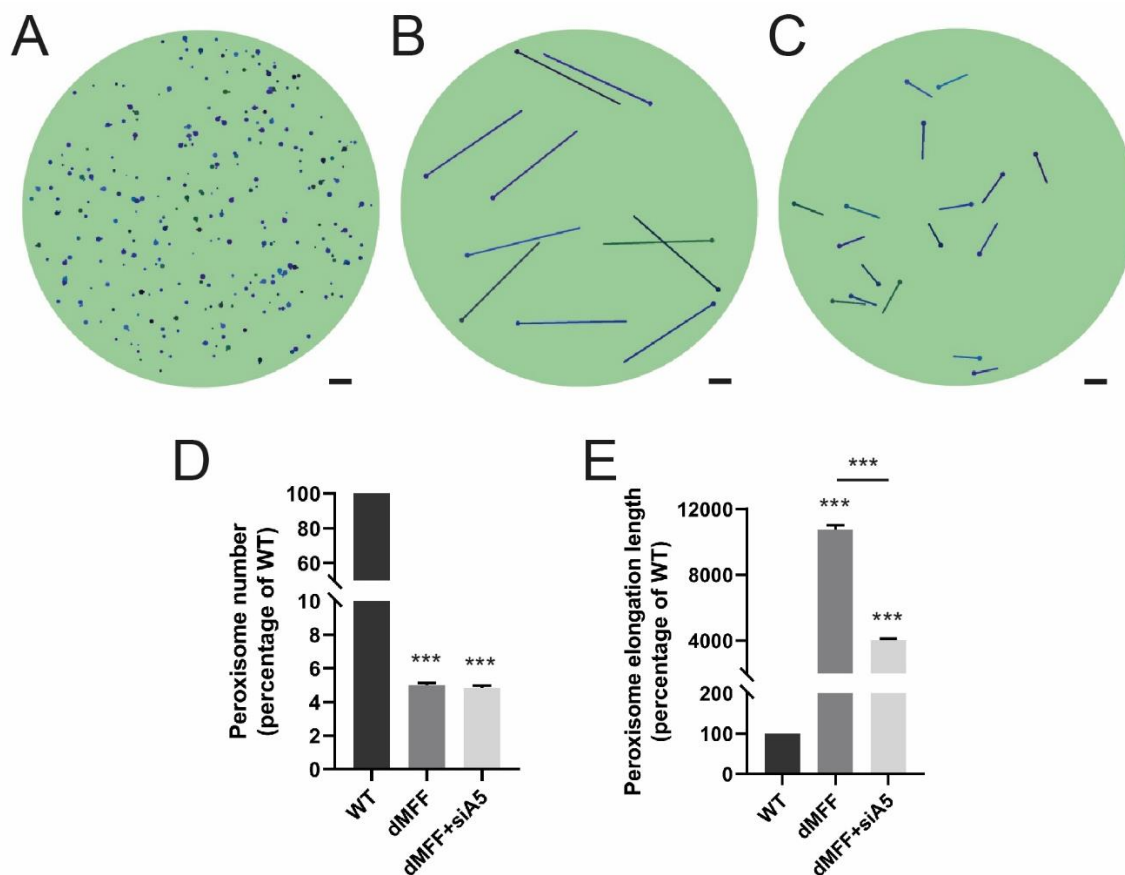
748 It is suggested that a block in peroxisome fission (e.g., due to mutations in MFF or DRP1), which results  
749 in the formation of larger, elongated organelles, may have deleterious effects on the mobility of  
750 peroxisomes, on synaptic homeostasis, and pexophagy (Schrader et al. 2014). We show here that highly  
751 elongated peroxisomes in MFF-deficient fibroblasts can be degraded by autophagic processes, which  
752 were induced by expression of a fragment of PEX3 [*HsPEX3*(1-44)] (Soukupova et al. 1999) or by  
753 amino acid starvation. Highly elongated mitochondria, for example, were reported to be spared from  
754 mitophagy under starvation conditions (Rambold et al. 2011; Gomes et al. 2011). Our data reveal that

755 elongated peroxisomes are not spared from autophagic processes, e.g. due to physical limitations, and  
756 indicate that impaired peroxisome degradation may not contribute to the pathology of MFF-deficiency.  
757 However, degradation of elongated peroxisomes in MFF-deficient cells may be slower than in control  
758 cells containing predominantly spherical peroxisomes, as tubules may need to shorten/fragment prior  
759 to removal by autophagy. Interestingly, a shortening of elongated peroxisomes was observed during  
760 amino acid starvation in HBSS, which was accompanied by alterations in peroxisomal marker proteins,  
761 e.g. the PMPs ACBD5 and PEX11 $\beta$ , which are required for membrane expansion and elongation.  
762 PEX11 $\beta$  mediates membrane deformation and elongation of the peroxisomal membrane (Delille et al.  
763 2010; Opaliński et al. 2011), whereas ACBD5 has recently been shown to mediate membrane contact  
764 sites between peroxisomes and the ER by interacting with ER-resident VAP proteins (Costello et al.  
765 2017b; Hua et al. 2017). Depletion of ACBD5 (or VAP) in MFF-deficient fibroblasts resulted in a  
766 shortening of elongated peroxisomes, likely due to disruption of the peroxisome-ER contact sites and  
767 reduced transfer of lipids from the ER to peroxisomes, which are required for peroxisomal membrane  
768 expansion (Costello et al. 2017b; Schrader et al. 2019). Our findings are in line with these previous  
769 observations and indicate that elongated peroxisomes in MFF-deficient cells are not fully static, but still  
770 dynamic under certain conditions. It is possible that a shortening/fragmentation of elongated  
771 peroxisomes under conditions of amino acid starvation facilitates their subsequent removal by  
772 autophagy.

773 Mitochondrial and peroxisomal dynamics are particularly important for brain development and function  
774 (Berger et al. 2016; Khacho and Slack 2018), likely explaining why MFF-deficient patients show  
775 primarily neurological defects. In contrast to the more prevalent neurological features in human patients  
776 with MFF-deficiency, mice without MFF die of heart failure at week 13, as a result of severe  
777 cardiomyopathy, which is likely based on mitochondrial alterations (Chen et al. 2015). However,  
778 removal of MFF exacerbated neuronal loss, astrogliosis and neuroinflammation in a Huntington's  
779 disease mouse model (Cha et al. 2018). Similar to patient fibroblasts, peroxisomes (and mitochondria)  
780 in MFF-deficient mouse embryonic fibroblasts were highly elongated (Chen et al. 2015). Interestingly,  
781 peroxisomal length was not substantially altered in MFF-deficient mouse cardiomyocytes (Chen et al.  
782 2015). This strongly indicates that peroxisome morphology and division is affected in a cell type-  
783 specific manner.

784 We recently developed a mathematical model to explain and predict alterations in peroxisome  
785 morphology and dynamics in health and disease conditions (Castro et al. 2018). In this stochastic,  
786 population-based modelling approach, each individual peroxisome consists of a spherical body with an  
787 optional cylindrical elongation. Peroxisome shape (i.e. the body radius and elongation length) are  
788 determined by (i) membrane lipid flow into the body (e.g., from the ER) (governed by rate  $\alpha$  and lipid  
789 flow constant  $\gamma$ ), (ii) elongation growth (governed by speed  $v$  and minimum body radius  $r_{min}$ ) and (iii)  
790 peroxisome division with a rate proportional to the elongation length (governed by rate  $\beta$  and minimum  
791 length  $L_{min}$ ). Peroxisome turnover is controlled by the peroxisome mean lifetime  $\tau$ . We recently  
792 demonstrated that this model is applicable to a range of experimental and disease conditions, e.g. loss  
793 of PEX5 in Zellweger spectrum disorders (Castro et al. 2018). With wild-type parameters, peroxisomes  
794 in the model are typically high in number, with only a low percentage showing elongations, all of which  
795 are short (**Fig. 6A**). The morphological alterations of peroxisomes in MFF-deficient fibroblasts that we  
796 have observed experimentally are captured by changing only one parameter, namely by reducing the  
797 division rate  $\beta$  to almost zero (**Fig. 6B**). As the membrane lipid flow rate and elongation growth speed  
798 remain unchanged, this results in reduced numbers of peroxisomes with significantly longer membrane  
799 elongations (**Fig. 6D, E**). The observation that control fibroblasts display large numbers of small,  
800 spherical peroxisomes, but turn into few, extremely elongated organelles upon blocking of peroxisomal

801 division, indicates that membrane lipid flow rate, elongation growth speed and division rate must be  
 802 high in fibroblasts under normal conditions. In contrast, low membrane lipid flow rate or elongation  
 803 speed in other cell types may result in a population of small peroxisomes and reduced numbers. This is  
 804 reflected by depletion of ACBD5, which impacts on peroxisome-ER tethering and membrane expansion,  
 805 resulting in shorter peroxisomes in MFF-deficient cells (Costello et al. 2017b). This morphological  
 806 change can also be captured in the model by reducing the lipid flow rate  $\alpha$  in addition to the division  
 807 rate  $\beta$  (**Fig. 6C-E**). It is thus likely that peroxisome morphology is differently affected in various cell  
 808 types in MFF-deficient patients. It should also be considered that environmental changes and related  
 809 signalling events that trigger peroxisomal membrane expansion and division (e.g. metabolic alterations  
 810 and certain stress conditions) can potentially promote the formation of hyper-elongated peroxisomes in  
 811 formerly unaffected cell types and contribute to the pathophysiology of MFF-deficiency.  
 812



813

814 **Figure 6.** A mathematical model of peroxisome morphology and dynamics in wild-type and MFF-  
 815 deficient patient fibroblasts. **(A)** Snapshot of model simulation for wild-type cells at  $t = 300$  hours  
 816 ( $\alpha = 100 \text{ nm}^2/\text{s}$ ,  $\beta = 2 \times 10^{-5}/\text{nm}/\text{s}$ ,  $v = 0.3 \text{ nm}/\text{s}$ ,  $\tau = 4 \times 10^5 \text{ s}$ ,  $\gamma = 2.5 \times 10^{-7}/\text{nm}^2$ ). **(B)** Snapshot of model  
 817 simulation of MFF-deficient cells (dMFF) at  $t = 300$  hours ( $\alpha = 100 \text{ nm}^2/\text{s}$ ,  $\beta = 2 \times 10^{-15}/\text{nm}/\text{s}$ ,  
 818  $v = 0.3 \text{ nm}/\text{s}$ ,  $\tau = 4 \times 10^5 \text{ s}$ ,  $\gamma = 2.5 \times 10^{-7}/\text{nm}^2$ ). **(C)** Snapshot of model simulation of MFF-deficient cells  
 819 with reduced lipid flow to simulate silencing of ACBD5 (siA5) at  $t = 300$  hours ( $\alpha = 5 \text{ nm}^2/\text{s}$ ,  
 820  $\beta = 2 \times 10^{-15}/\text{nm}/\text{s}$ ,  $v = 0.3 \text{ nm}/\text{s}$ ,  $\tau = 4 \times 10^5 \text{ s}$ ,  $\gamma = 2.5 \times 10^{-7}/\text{nm}^2$ ). **(D)** Average peroxisome number at  $t$   
 821  $= 300$  hours of simulations shown in **A-C**, represented as percentages relative to WT ( $n = 100$ ). **(E)**  
 822 Average non-zero peroxisome elongation length at  $t = 300$  hours of simulations shown in **A-C**,  
 823 represented as percentages relative to WT ( $n = 100$ ). Scale bars,  $1 \mu\text{m}$ .



## 824 **5. Additional Information**

### 825 **5.1. Acknowledgements**

826 We would like to thank F.S. Alkuraya, King Faisal Specialist Hospital and Research Center, Riyadh,  
827 Saudi Arabia for providing patient skin fibroblasts, and M. Schuster for support with FRAP experiments.  
828 This work was supported by the Biotechnology and Biological Sciences Research Council (BBSRC)  
829 (BB/N01541X/1, BB/R016844/1; to M.S.), the European Union's Horizon 2020 research and  
830 innovation programme under the Marie Skłodowska-Curie grant agreement No 812968 PERICO (to  
831 M.S., M.F.), and the Research Foundation – Flanders (G095315N; to M.F.). M.I. was supported by the  
832 German Research Foundation (DFG Grant 397476530) and MEAMEDMA Anschubförderung,  
833 Medical Faculty Mannheim, University of Heidelberg. Y.W. was supported by the German Research  
834 Foundation (DFG Grant D10043030, SFB 1134 – Functional Ensembles). D.M.R. gratefully  
835 acknowledges financial support from the Medical Research Council (MR/P022405/1) and the  
836 Wellcome Trust Institutional Strategic Support Award (WT105618MA). C.L. was supported by the KU  
837 Leuven (PDM/18/188) and the Research Foundation – Flanders (1213620N). Support grants to J.P.  
838 were provided by Zellweger UK, The Sidney Perry Foundation and The Devon Educational Trust.

839 The research data supporting this publication are provided within this paper and as supplementary  
840 information.

841 The authors declare no competing financial interests.

### 842 **5.2. Author Contributions**

843 JP, RC, TS, LG, SF, CL, YW, CH, MI, DR, MS performed experiments and analysed data. MS, SF, PF,  
844 MF, MI conceived the project and analysed data. JP, MS wrote the manuscript. All authors contributed  
845 to methods.

## 846 **6. References**

- 847 Anding AL, Baehrecke EH (2017) Cleaning house: selective autophagy of organelles. *Dev Cell*  
848 41:10–22. <https://doi.org/10.1016/j.devcel.2017.02.016>
- 849 Arias JA, Moser AB, Goldfischer SL (1985) Ultrastructural and cytochemical demonstration of  
850 peroxisomes in cultured fibroblasts from patients with peroxisomal deficiency disorders. *J Cell*  
851 *Biol* 100:1789–92. <https://doi.org/10.1083/jcb.100.5.1789>
- 852 Asare A, Levorse J, Fuchs E (2017) Coupling organelle inheritance with mitosis to balance growth  
853 and differentiation. *Science* (80- ) 355:eaah4701. <https://doi.org/10.1126/science.aah4701>
- 854 Barros-Barbosa A, Ferreira MJ, Rodrigues TA, et al (2019) Membrane topologies of PEX13 and  
855 PEX14 provide new insights on the mechanism of protein import into peroxisomes. *FEBS J*  
856 286:205–222. <https://doi.org/10.1111/febs.14697>
- 857 Berger J, Dorninger F, Forss-Petter S, Kunze M (2016) Peroxisomes in brain development and  
858 function. *Biochim Biophys Acta - Mol Cell Res* 1863:934–955.  
859 <https://doi.org/10.1016/j.bbamcr.2015.12.005>
- 860 Bharti P, Schliebs W, Schievelbusch T, et al (2011) PEX14 is required for microtubule-based  
861 peroxisome motility in human cells. *J Cell Sci* 124:1759–1768.  
862 <https://doi.org/10.1242/jcs.079368>
- 863 Bonekamp NA, Islinger M, Lázaro MG, Schrader M (2013) Cytochemical detection of peroxisomes  
864 and mitochondria. *Methods Mol Biol* 931:467–482. [https://doi.org/10.1007/978-1-62703-056-4\\_24](https://doi.org/10.1007/978-1-62703-056-4_24)  
865
- 866 Braverman NE, Raymond G V, Rizzo WB, et al (2016) Peroxisome biogenesis disorders in the  
867 Zellweger spectrum: An overview of current diagnosis, clinical manifestations, and treatment  
868 guidelines. *Mol Genet Metab* 117:313–21. <https://doi.org/10.1016/j.ymgme.2015.12.009>
- 869 Brown L-A, Baker A (2008) Shuttles and cycles: transport of proteins into the peroxisome matrix  
870 (review). *Mol Membr Biol* 25:363–375. <https://doi.org/10.1080/09687680802130583>
- 871 Castro IG, Richards DM, Metz J, et al (2018) A role for Mitochondrial Rho GTPase 1 (MIRO1) in  
872 motility and membrane dynamics of peroxisomes. *Traffic* 19:229–242.  
873 <https://doi.org/10.1111/tra.12549>
- 874 Cepińska MN, Veenhuis M, van der Klei IJ, Nagotu S (2011) Peroxisome fission is associated with  
875 reorganization of specific membrane proteins. *Traffic* 12:925–37. <https://doi.org/10.1111/j.1600-0854.2011.01198.x>  
876
- 877 Cha MY, Chen H, Chan D (2018) Removal of the mitochondrial fission factor Mff exacerbates  
878 neuronal loss and neurological phenotypes in a Huntington’s Disease mouse model. *PLoS Curr*  
879 10:. <https://doi.org/10.1371/currents.hd.a4e15b80c4915c828d39754942c6631f>
- 880 Chen H, Ren S, Clish C, et al (2015) Titration of mitochondrial fusion rescues Mff-deficient  
881 cardiomyopathy. *J Cell Biol* 211:795–805. <https://doi.org/10.1083/jcb.201507035>
- 882 Costello JL, Castro IG, Camões F, et al (2017a) Predicting the targeting of tail-anchored proteins to  
883 subcellular compartments in mammalian cells. *J Cell Sci* 130:1675–1687.  
884 <https://doi.org/10.1242/jcs.200204>
- 885 Costello JL, Castro IG, Hacker C, et al (2017b) ACBD5 and VAPB mediate membrane associations  
886 between peroxisomes and the ER. *J Cell Biol* 216:331–342.  
887 <https://doi.org/10.1083/jcb.201607055>

- 888 Costello JL, Passmore JB, Islinger M, Schrader M (2018) Multi-localized proteins: the peroxisome-  
889 mitochondria connection. In: Sub-cellular biochemistry. pp 383–415
- 890 Covill-Cooke C, Toncheva VS, Drew J, et al (2020) Peroxisomal fission is modulated by the  
891 mitochondrial Rho-GTPases, Miro1 and Miro2. *EMBO Rep* 21:.  
892 <https://doi.org/10.15252/embr.201949865>
- 893 Coyle B, Kinsella P, McCann M, et al (2004) Induction of apoptosis in yeast and mammalian cells by  
894 exposure to 1,10-phenanthroline metal complexes. *Toxicol Vitro* 18:63–70.  
895 <https://doi.org/10.1016/j.tiv.2003.08.011>
- 896 Dacremont G, Cocquyt G, Vincent G (1995) Measurement of very long-chain fatty acids, phytanic  
897 and pristanic acid in plasma and cultured fibroblasts by gas chromatography. *J Inher Metab Dis*  
898 18 Suppl 1:76–83. <https://doi.org/10.1007/bf00711430>
- 899 Dansen TB, Wirtz KWA, Wanders RJA, Pap EHW (2000) Peroxisomes in human fibroblasts have a  
900 basic pH. *Nat Cell Biol* 2:51–53. <https://doi.org/10.1038/71375>
- 901 Delille HK, Agricola B, Guimaraes SC, et al (2010) Pex11p $\beta$ -mediated growth and division of  
902 mammalian peroxisomes follows a maturation pathway. *J Cell Sci* 123:2750–2762.  
903 <https://doi.org/10.1242/jcs.062109>
- 904 Dorninger F, Forss-Petter S, Berger J (2017) From peroxisomal disorders to common  
905 neurodegenerative diseases - the role of ether phospholipids in the nervous system. *FEBS Lett*  
906 591:2761–2788. <https://doi.org/10.1002/1873-3468.12788>
- 907 Ebberink MS, Koster J, Visser G, et al (2012) A novel defect of peroxisome division due to a  
908 homozygous non-sense mutation in the PEX11 $\beta$  gene. *J. Med. Genet.* 49:307–313
- 909 Eberhart T, Kovacs WJ (2018) Pexophagy in yeast and mammals: an update on mysteries. *Histochem*  
910 *Cell Biol* 150:473–488. <https://doi.org/10.1007/s00418-018-1724-3>
- 911 Ferdinandusse S, Ebberink MS, Vaz FM, et al (2016) The important role of biochemical and  
912 functional studies in the diagnostics of peroxisomal disorders. *J Inher Metab Dis* 39:531–543.  
913 <https://doi.org/10.1007/s10545-016-9922-4>
- 914 Francisco T, Rodrigues TA, Dias AF, et al (2017) Protein transport into peroxisomes: Knowns and  
915 unknowns. *BioEssays* 39:1700047. <https://doi.org/10.1002/bies.201700047>
- 916 Fransen M, Lismont C (2018) Peroxisomes and cellular oxidant/antioxidant balance: protein redox  
917 modifications and impact on inter-organelle communication. In: Sub-cellular biochemistry. pp  
918 435–461
- 919 Fransen M, Lismont C (2019) Redox signaling from and to peroxisomes: progress, challenges, and  
920 prospects. *Antioxid Redox Signal* 30:95–112. <https://doi.org/10.1089/ars.2018.7515>
- 921 Fransen M, Wylín T, Brees C, et al (2001) Human pex19p binds peroxisomal integral membrane  
922 proteins at regions distinct from their sorting sequences. *Mol Cell Biol* 21:4413–24.  
923 <https://doi.org/10.1128/MCB.21.13.4413-4424.2001>
- 924 Galiani S, Waithe D, Reglinski K, et al (2016) Super-resolution microscopy reveals  
925 compartmentalization of peroxisomal membrane proteins. *J Biol Chem* 291:16948–62.  
926 <https://doi.org/10.1074/jbc.M116.734038>
- 927 Gandre-Babbe S, van der Blik AM (2008) The novel tail-anchored membrane protein Mff controls  
928 mitochondrial and peroxisomal fission in mammalian cells. *Mol Biol Cell* 19:2402–2412.  
929 <https://doi.org/10.1091/mbc.E07>

- 930 Gerber S, Charif M, Chevrollier A, et al (2017) Mutations in DNMI1L, as in OPA1, result in dominant  
931 optic atrophy despite opposite effects on mitochondrial fusion and fission. *Brain* 140:2586–2596.  
932 <https://doi.org/10.1093/brain/awx219>
- 933 Godinho LF, Schrader M (2017) Determination of peroxisomal pH in living mammalian cells using  
934 pHRed. In: *Methods in molecular biology* (Clifton, N.J.). pp 181–189
- 935 Gomes LC, Benedetto G Di, Scorrano L (2011) During autophagy mitochondria elongate, are spared  
936 from degradation and sustain cell viability. *Nat Cell Biol* 13:589–598.  
937 <https://doi.org/10.1038/ncb2220>
- 938 Helle SCJ, Feng Q, Aebersold MJ, et al (2017) Mechanical force induces mitochondrial fission. *Elife*  
939 6:. <https://doi.org/10.7554/eLife.30292>
- 940 Hua R, Cheng D, Coyaud É, et al (2017) VAPs and ACBD5 tether peroxisomes to the ER for  
941 peroxisome maintenance and lipid homeostasis. *J Cell Biol* 216:367–377.  
942 <https://doi.org/10.1083/jcb.201608128>
- 943 Huber N, Guimaraes S, Schrader M, et al (2013) Charcot-Marie-Tooth disease-associated mutants of  
944 GDAP1 dissociate its roles in peroxisomal and mitochondrial fission. *EMBO Rep* 14:545–552.  
945 <https://doi.org/10.1038/embor.2013.56>
- 946 Itoyama A, Michiyuki S, Honsho M, et al (2013) Mff functions with Pex11p and DLP1 in  
947 peroxisomal fission. *Biol Open*. <https://doi.org/10.1242/bio.20135298>
- 948 Ivashchenko O, Van Veldhoven PP, Brees C, et al (2011) Intraperoxisomal redox balance in  
949 mammalian cells: oxidative stress and interorganellar cross-talk. *Mol Biol Cell* 22:1440–1451.  
950 <https://doi.org/10.1091/mbc.E10-11-0919>
- 951 Jo DS, Bae D-J, Park SJ, et al (2015) Pexophagy is induced by increasing peroxisomal reactive  
952 oxygen species in 1'10-phenanthroline-treated cells. *Biochem Biophys Res Commun* 467:354–  
953 360. <https://doi.org/10.1016/j.bbrc.2015.09.153>
- 954 Kemp S, Valianpour F, Mooyer PAW, et al (2004) Method for measurement of peroxisomal very-  
955 long-chain fatty acid beta-oxidation in human skin fibroblasts using stable-isotope-labeled  
956 tetracosanoic acid. *Clin Chem* 50:1824–6. <https://doi.org/10.1373/clinchem.2004.038539>
- 957 Khacho M, Slack RS (2018) Mitochondrial dynamics in the regulation of neurogenesis: From  
958 development to the adult brain. *Dev Dyn* 247:47–53. <https://doi.org/10.1002/dvdy.24538>
- 959 Koch A, Schneider G, Lüers GH, Schrader M (2004) Peroxisome elongation and constriction but not  
960 fission can occur independently of dynamin-like protein 1. *J Cell Sci* 117:3995–4006.  
961 <https://doi.org/10.1242/jcs.01268>
- 962 Koch A, Yoon Y, Bonekamp NA, et al (2005) A role for Fis1 in both mitochondrial and peroxisomal  
963 fission in mammalian cells. *Mol Biol Cell* 16:5077–5086. <https://doi.org/10.1091/mbc.E05>
- 964 Koch J, Brocard C (2012) PEX11 proteins attract Mff and hFis1 to coordinate peroxisomal fission. *J*  
965 *Cell Sci* 125:3813–3826. <https://doi.org/https://doi.org/10.1242/jcs.102178>
- 966 Koch J, Feichtinger RG, Freisinger P, et al (2016) Disturbed mitochondrial and peroxisomal dynamics  
967 due to loss of MFF causes Leigh-like encephalopathy, optic atrophy and peripheral neuropathy.  
968 *J Med Genet* 53:270–278. <https://doi.org/10.1136/jmedgenet-2015-103500>
- 969 Ladds E, Whitney A, Dombi E, et al (2018) De novo DNMI1L mutation associated with mitochondrial  
970 epilepsy syndrome with fever sensitivity. *Neurol Genet* 4:e258.  
971 <https://doi.org/10.1212/NXG.0000000000000258>

- 972 Lasorsa FM, Pinton P, Palmieri L, et al (2008) Peroxisomes as novel players in cell calcium  
973 homeostasis. *J Biol Chem* 283:15300–15308. <https://doi.org/10.1074/jbc.M800648200>
- 974 Lee MY, Sumpter R, Zou Z, et al (2017) Peroxisomal protein PEX13 functions in selective  
975 autophagy. *EMBO Rep* 18:48–60. <https://doi.org/10.15252/embr.201642443>
- 976 Lewis TL, Kwon S-K, Lee A, et al (2018) MFF-dependent mitochondrial fission regulates presynaptic  
977 release and axon branching by limiting axonal mitochondria size. *Nat Commun* 9:5008.  
978 <https://doi.org/10.1038/s41467-018-07416-2>
- 979 Lismont C, Koster J, Provost S, et al (2019a) Deciphering the potential involvement of PXMP2 and  
980 PEX11B in hydrogen peroxide permeation across the peroxisomal membrane reveals a role for  
981 PEX11B in protein sorting. *Biochim Biophys Acta - Biomembr*.  
982 <https://doi.org/10.1016/J.BBAMEM.2019.05.013>
- 983 Lismont C, Nordgren M, Brees C, et al (2019b) Peroxisomes as modulators of cellular protein thiol  
984 oxidation: a new model system. *Antioxid Redox Signal* 30:22–39.  
985 <https://doi.org/10.1089/ars.2017.6997>
- 986 Lismont C, Walton PA, Fransen M (2017) Quantitative monitoring of subcellular redox dynamics in  
987 living mammalian cells using roGFP2-based probes. In: *Methods in molecular biology* (Clifton,  
988 N.J.). pp 151–164
- 989 Long B, Wang K, Li N, et al (2013) MiR-761 regulates the mitochondrial network by targeting  
990 mitochondrial fission factor. *Free Radic Biol Med* 65:371–9.  
991 <https://doi.org/10.1016/j.freeradbiomed.2013.07.009>
- 992 Nasca A, Legati A, Baruffini E, et al (2016) Biallelic mutations in DNMI1L are associated with a  
993 slowly progressive infantile encephalopathy. *Hum Mutat* 37:898–903.  
994 <https://doi.org/10.1002/humu.23033>
- 995 Nasca A, Nardecchia F, Commone A, et al (2018) Clinical and biochemical features in a patient with  
996 mitochondrial fission factor gene alteration. *Front Genet* 9:625.  
997 <https://doi.org/10.3389/fgene.2018.00625>
- 998 Ofman R, Wanders RJ (1994) Purification of peroxisomal acyl-CoA: dihydroxyacetonephosphate  
999 acyltransferase from human placenta. *Biochim Biophys Acta* 1206:27–34
- 1000 Okumoto K, Ono T, Toyama R, et al (2018) New splicing variants of mitochondrial Rho GTPase-1  
1001 (Miro1) transport peroxisomes. *J Cell Biol* 217:619–633. <https://doi.org/10.1083/jcb.201708122>
- 1002 Opaliński L, Kiel JAKW, Williams C, et al (2011) Membrane curvature during peroxisome fission  
1003 requires Pex11. *EMBO J* 30:5–16. <https://doi.org/10.1038/emboj.2010.299>
- 1004 Palmer CS, Elgass KD, Parton RG, et al (2013) Adaptor proteins MiD49 and MiD51 can act  
1005 independently of Mff and Fis1 in Drp1 recruitment and are specific for mitochondrial fission. *J*  
1006 *Biol Chem* 288:27584–93. <https://doi.org/10.1074/jbc.M113.479873>
- 1007 Rambold AS, Kostecky B, Elia N, Lippincott-schwartz J (2011) Tubular network formation protects  
1008 mitochondria from autophagosomal degradation during nutrient starvation. *Proc Natl Acad Sci*  
1009 *U S A* 108:10190–10195. <https://doi.org/10.1073/pnas.1107402108>
- 1010 Raymond G V, Moser AB, Fatemi A (1993) X-Linked Adrenoleukodystrophy
- 1011 Ribeiro D, Castro I, Fahimi HD, Schrader M (2012) Peroxisome morphology in pathology. *Histol*  
1012 *Histopathol* 27:661–676
- 1013 Rottensteiner H, Theodoulou FL (2006) The ins and outs of peroxisomes: co-ordination of membrane

- 1014 transport and peroxisomal metabolism. *Biochim Biophys Acta (BBA)-Molecular Cell Res*  
1015 1763:1527–1540. <https://doi.org/10.1016/j.bbamcr.2006.08.012>
- 1016 Sargent G, van Zutphen T, Shatseva T, et al (2016) PEX2 is the E3 ubiquitin ligase required for  
1017 pexophagy during starvation. *J Cell Biol* 214:677–690. <https://doi.org/10.1083/jcb.201511034>
- 1018 Schneider CA, Rasband WS, Eliceiri KW (2012) NIH Image to ImageJ: 25 years of image analysis.  
1019 *Nat Methods* 9:671–5. <https://doi.org/10.1038/nmeth.2089>
- 1020 Schrader M, Bonekamp NA, Islinger M (2012) Fission and proliferation of peroxisomes. *Biochim*  
1021 *Biophys Acta - Mol Basis Dis* 1822:1343–1357. <https://doi.org/10.1016/j.bbadis.2011.12.014>
- 1022 Schrader M, Castro I, Fahimi HD, Islinger M (2014) Peroxisome morphology in pathologies. In:  
1023 *Molecular Machines Involved in Peroxisome Biogenesis and Maintenance*. Springer, pp 125–  
1024 151
- 1025 Schrader M, Costello JL, Godinho LF, et al (2016) Proliferation and fission of peroxisomes - An  
1026 update. *Biochim Biophys Acta - Mol Cell Res* 1863:971–983.  
1027 <https://doi.org/10.1016/j.bbamcr.2015.09.024>
- 1028 Schrader M, Kamoshita M, Islinger M (2019) Organelle interplay-peroxisome interactions in health  
1029 and disease. *J Inherit Metab Dis*. <https://doi.org/10.1002/jimd.12083>
- 1030 Schrader M, Thiemann M, Fahimi HD (2003) Peroxisomal Motility and Interaction With  
1031 Microtubules. *Microsc Res Tech* 61:171–178. <https://doi.org/10.1002/jemt.10326>
- 1032 Schrader TA, Schrader M (2017) SiRNA-mediated silencing of peroxisomal genes in mammalian  
1033 cells. In: *Methods in molecular biology (Clifton, N.J.)*. pp 69–79
- 1034 Schuster M, Kilaru S, Ashwin P, et al (2011a) Controlled and stochastic retention concentrates dynein  
1035 at microtubule ends to keep endosomes on track. *EMBO J* 30:652–664.  
1036 <https://doi.org/10.1038/emboj.2010.360>
- 1037 Schuster M, Lipowsky R, Assmann MA, et al (2011b) Transient binding of dynein controls  
1038 bidirectional long-range motility of early endosomes. *Proc Natl Acad Sci U S A* 108:3618–3623.  
1039 <https://doi.org/10.1073/pnas.1015839108>
- 1040 Shamseldin HE, Alshammari M, Al-Sheddi T, et al (2012) Genomic analysis of mitochondrial  
1041 diseases in a consanguineous population reveals novel candidate disease genes. *J Med Genet*  
1042 49:234–241. <https://doi.org/10.1136/jmedgenet-2012-100836>
- 1043 Soliman K, Göttfert F, Rosewich H, et al (2018) Super-resolution imaging reveals the sub-diffraction  
1044 phenotype of Zellweger Syndrome ghosts and wild-type peroxisomes. *Sci Rep* 8:7809.  
1045 <https://doi.org/10.1038/s41598-018-24119-2>
- 1046 Soukupova M, Sprenger C, Gorgas K, et al (1999) Identification and characterization of the human  
1047 peroxin PEX3. *Eur J Cell Biol* 78:357–374. [https://doi.org/10.1016/S0171-9335\(99\)80078-8](https://doi.org/10.1016/S0171-9335(99)80078-8)
- 1048 Tantama M, Hung YP, Yellen G (2011) Imaging intracellular pH in live cells with a genetically  
1049 encoded red fluorescent protein sensor. *J Am Chem Soc* 133:10034–10037.  
1050 <https://doi.org/10.1021/ja202902d>
- 1051 Taylor RL, Handley MT, Waller S, et al (2017) Novel PEX11B mutations extend the peroxisome  
1052 biogenesis disorder 14B phenotypic spectrum and underscore congenital cataract as an early  
1053 feature. *Invest Ophthalmol Vis Sci* 58:594–603. <https://doi.org/10.1167/iovs.16-21026>
- 1054 Theiss C, Neuhaus A, Schliebs W, Erdmann R (2012) TubStain: a universal peptide-tool to label  
1055 microtubules. *Histochem Cell Biol* 138:531–540. <https://doi.org/10.1007/s00418-012-0992-6>

- 1056 Thiemann M, Schrader M, Volkl A, et al (2000) Interaction of peroxisomes with microtubules In vitro  
1057 studies using a novel peroxisome-microtubule binding assay. *Eur J Biochem* 267:6264–6275.  
1058 <https://doi.org/10.1046/j.1432-1327.2000.01713.x>
- 1059 van Roermund CWT, de Jong M, IJlst L, et al (2004) The peroxisomal lumen in *Saccharomyces*  
1060 *cerevisiae* is alkaline. *J Cell Sci* 117:4231–7. <https://doi.org/10.1242/jcs.01305>
- 1061 Vanstone JR, Smith AM, McBride S, et al (2016) DNM1L-related mitochondrial fission defect  
1062 presenting as refractory epilepsy. *Eur J Hum Genet* 24:1084–1088.  
1063 <https://doi.org/10.1038/ejhg.2015.243>
- 1064 Wanders RJ, Denis S, Ruiten JP, et al (1995) Measurement of peroxisomal fatty acid beta-oxidation in  
1065 cultured human skin fibroblasts. *J Inherit Metab Dis* 18 Suppl 1:113–24.  
1066 <https://doi.org/10.1007/bf00711434>
- 1067 Wanders RJ, Van Roermund CW (1993) Studies on phytanic acid alpha-oxidation in rat liver and  
1068 cultured human skin fibroblasts. *Biochim Biophys Acta* 1167:345–50.  
1069 [https://doi.org/10.1016/0005-2760\(93\)90239-6](https://doi.org/10.1016/0005-2760(93)90239-6)
- 1070 Wanders RJA (2018) Peroxisomal disorders: Improved laboratory diagnosis, new defects and the  
1071 complicated route to treatment. *Mol Cell Probes* 40:60–69.  
1072 <https://doi.org/10.1016/j.mcp.2018.02.001>
- 1073 Waterham HR, Koster J, van Roermund CWT, et al (2007) A lethal defect of mitochondrial and  
1074 peroxisomal fission. *N Engl J Med* 356:1736–1741.  
1075 <https://doi.org/https://doi.org/10.1056/NEJMoa064436>
- 1076 Williams C, Opalinski L, Landgraf C, et al (2015) The membrane remodeling protein Pex11p  
1077 activates the GTPase Dnm1p during peroxisomal fission. *Proc Natl Acad Sci U S A* 112:6377–  
1078 6382. <https://doi.org/10.1073/pnas.1418736112>
- 1079 Yoon G, Malam Z, Paton T, et al (2016) Lethal disorder of mitochondrial fission caused by mutations  
1080 in DNM1L. *J Pediatr* 171:313-316.e2. <https://doi.org/10.1016/j.jpeds.2015.12.060>
- 1081
- 1082